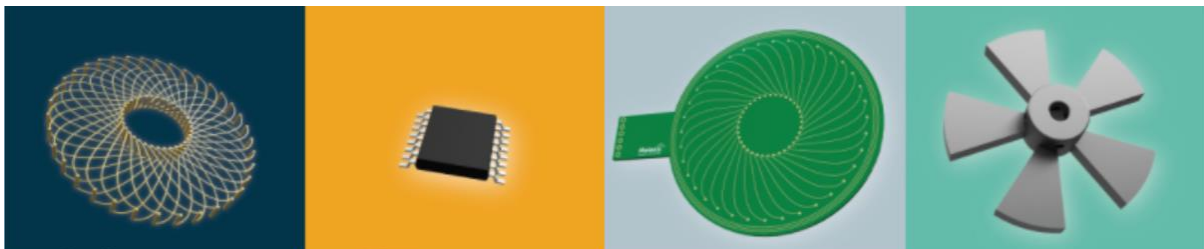


## Ludovic Mbengué Matanga

**Master Nanotech**  
**2021-2022**

**Melexis Technologies SA**  
Chem. de Buchaux 38, 2022 Bevaix, Switzerland

Performance evaluation and comparison of different  
inductive sensor-based position sensing approaches  
from 14/02/2022 to 14/08/2022



Confidentiality: **yes** no

**Under the supervision of:**

- **Company supervisor: Yassine Akermi, yae@melexis.com**
- **Phelma Tutor: Prof. Liliana PREJBEANU, liliana.buda@cea.fr**

**Ecole nationale  
supérieure de physique,  
électronique, matériaux**

**Phelma**  
Bât. Grenoble INP - Minatec  
3 Parvis Louis Néel - CS 50257  
F-38016 Grenoble Cedex 01

Tél +33 (0)4 56 52 91 00  
Fax +33 (0)4 56 52 91 3

<http://phelma.grenoble-inp.fr>

# Acknowledgements

First of all, I would like to thank Grenoble INP Phelma, and particularly Ms. PREJBEANU Liliana, for having placed their trust in me. The support and guidance I received enabled me to quickly find an internship, with the goal of refining my professional project and obtaining my engineering degree from the Institut National Polytechnique de Grenoble, specializing in micro and nanotechnologies for integrated systems.

I also think of Mr. Alexandre Boillat, Melexis Regional Site Manager France & Switzerland, who believed in my potential and welcomed me into his company.

In this respect, I would like to thank in particular Mr. Yassine Akermi, Applications Engineer for Inductive Sensors, who supported me, advised me and above all transmitted his expertise in the field of inductive position sensors. As well as his team, notably Seriem Sid-Ahmed, Applications Engineer for Inductive Sensors, and Lorenzo Lugani, Product Manager for Inductive Sensors.

This internship allowed me to refine some of my professional plans and the beginning of my career. It also marked the end of my university studies.

I would also like to thank my family and friends who have constantly supported me in the elaboration of my professional project and helped me at each step of this internship report. Special thanks to my proofreader and corrector who contributed, thanks to his advice and recommendations, to the development and smooth running of my internship report.

## Abstract

The purpose of this internship at Melexis is to evaluate different position sensing approaches based on inductive technology.

In summary, I studied and compared different inductive IC interfaces for position measurement, implemented different algorithms to be able to evaluate the various measurement approaches, planned and performed measurement campaigns to evaluate each approach.

The objectives in scope of this internship are multiple. In a first instance, I simulated and modeled three different inductive position sensors. An O-shaped five Pole pairs sensor, a C-shaped five Pole pairs sensor and a small O-shaped one pole pair sensor for more specific applications. I have subsequently upgraded the measurement setup of the inductive lab, to be able to characterize two different versions of these sensors: The MLX90510 version and the MLX90517 one. This characterization consisted of the quantification of offsets, amplitudes and orthogonality errors for input and output signals. For a more complete analysis I did a performance evaluation of all sensors with variable airgaps and mechanical tolerances, and also a noise quantification at output for both solutions. Finally, as an additional analysis, I tried to evaluate the effect of the AGC (sensor gain) on the output signals of the MLX90517 (with airgap change and mechanical tolerances), the effect of speed on measurement precision and to compare these Melexis sensors with competition reference designs.

## Riassunto

Lo scopo di questo stage presso Melexis è valutare diversi approcci di rilevamento della posizione basati sulla tecnologia induttiva.

In sintesi, ho studiato e confrontato diverse interfacce IC induttive per la misurazione della posizione, implementato diversi algoritmi per poter valutare i vari approcci di misurazione, pianificato ed eseguito campagne di misurazione per valutare ogni approccio.

Gli obiettivi nell'ambito di questo tirocinio sono molteplici. In un primo caso, ho simulato e modellato tre diversi sensori di posizione induttivi. Un sensore a cinque coppie di poli a forma di O, un sensore a cinque coppie di poli a forma di C e un piccolo sensore a una coppia di poli a forma di O per applicazioni più specifiche. Successivamente ho aggiornato il setup di misura del laboratorio induttivo, per poter caratterizzare due diverse versioni di questi sensori: la versione MLX90510 e quella MLX90517. Questa caratterizzazione consisteva nella quantificazione di offset, ampiezze ed errori di ortogonalità per i segnali di ingresso e di uscita. Per un'analisi più completa ho effettuato una valutazione delle prestazioni di tutti i sensori con traferri variabili e tolleranze meccaniche, e anche una quantificazione del rumore in uscita per entrambe le soluzioni. Infine, come analisi aggiuntiva, ho provato a valutare l'effetto dell'AGC (guadagno del sensore) sui segnali di uscita dell'MLX90517 (con variazione del traferro e tolleranze meccaniche), l'effetto della velocità sulla precisione di misura e di confrontare questi sensori Melexis con progetti di riferimento del concorso.

## Résumé

L'objectif de ce stage chez Melexis est d'évaluer différentes approches de détection de position basées sur la technologie inductive.

En résumé, j'ai étudié et comparé différentes interfaces IC inductives pour la mesure de position, implémenté différents algorithmes pour pouvoir évaluer les différentes approches de mesure, planifié et réalisé des campagnes de mesure pour évaluer chaque approche.

Les objectifs visés par ce stage sont multiples. Dans un premier temps, j'ai simulé et modélisé trois capteurs de position inductifs différents. Un capteur à cinq paires de pôles en forme de O, un capteur à cinq paires de pôles en forme de C et un petit capteur à une paire de pôles en forme de O pour des applications plus spécifiques. J'ai par la suite fait évoluer le dispositif de mesure du laboratoire inductif, pour pouvoir caractériser deux versions différentes de ces capteurs : la version MLX90510 et la version MLX90517. Cette caractérisation consistait en la quantification des décalages, des amplitudes et des erreurs d'orthogonalité pour les signaux d'entrée et de sortie. Pour une analyse plus complète, j'ai fait une évaluation des performances de tous les capteurs avec des entrefers et des tolérances mécaniques variables, ainsi qu'une quantification du bruit en sortie pour les deux solutions. Enfin, comme analyse complémentaire, j'ai essayé d'évaluer l'effet de l'AGC (gain du capteur) sur les signaux de sortie du MLX90517 (avec changement d'entrefer et tolérances mécaniques), l'effet de la vitesse sur la précision de mesure et de comparer ces capteurs Melexis avec des conceptions de référence de compétition.

**Contents**

|       |  |    |
|-------|--|----|
| 1     | Introduction .....   | 5  |
| 2     | Inductive sensors.....   | 7  |
| 2.1   | General presentation.....  | 7  |
| 2.2   | Working principle of inductive position sensors.....                         | 8  |
| 2.3   | The four parts of the inductive sensor.....                                  | 8  |
| 2.3.1 | Coil-system and PCB.....   | 9  |
| 2.3.2 | Target.....  | 10 |
| 2.3.3 | Integrated Circuit.....  | 10 |
| 2.4   | Inductive sensing modes.....   | 12 |
| 2.5   | Error source of inductive sensors.....                                       | 13 |
| 3     | Project goal and timeline .....  | 15 |
| 3.1   | Project goal.....  | 15 |
| 3.2   | Project Timeline (The internship starts week 7 of 2022).....                 | 15 |
| 4     | Coil design and simulation .....   | 16 |
| 4.1   | O-shaped and C-shaped inductive position sensors: theory of coil design..... | 16 |
| 4.2   | Working principle .....  | 17 |
| 4.3   | O-shaped 5PP simulation results.....   | 18 |
| 4.4   | O-shaped 1PP simulation results.....   | 20 |
| 4.5   | C-shaped simulation results.....   | 22 |
| 4.6   | Conclusion .....   | 24 |
| 5     | Measures and MLX90510/MLX90517 evaluation .....                              | 24 |
| 5.1   | Measurement setup description.....   | 24 |
| 5.2   | Description of post processing algorithms .....                              | 26 |
| 5.3   | O-shaped (5PP) MLX90517 and MLX90510.....                                    | 27 |
| 5.3.1 | Measurement procedure, results and comparison with simulation.....           | 27 |
| 5.3.2 | Conclusion.....  | 36 |
| 5.4   | O-shaped (1PP) MLX90517 and MLX90510.....                                    | 37 |
| 5.4.1 | Measurement results and comparison with simulation.....                      | 37 |
| 5.4.2 | Conclusion.....  | 39 |
| 5.5   | C-shaped (5PP) MLX90510 and MLX90517.....                                    | 40 |
| 5.5.1 | Measurement results and comparison with simulation.....                      | 40 |
| 5.5.2 | Conclusion.....  | 43 |
| 5.6   | Conclusion .....   | 43 |
| 6     | Conclusions and perspectives.....  | 44 |
| 6.1   | Conclusion .....   | 44 |
| 6.2   | Personal review.....   | 44 |
| 7     | Bibliography.....  | 45 |

# 1 Introduction

Today the electric car market is booming. In 2035, because of new European laws, most car manufacturers will only sell electric vehicles. All manufacturers are then accelerating the development of their electric vehicle range with a view to major adoption. As a result, it is easy to understand that the market for on-board electronic sensors for the automobile is on the cusp of unprecedented growth. With the increasing electrification of motors comes the need to control them. There are several technological solutions to achieve this. However, an electric motor generates electromagnetic interferences to which it is advisable to associate a sensor which resists it. It is in a will to be able to control electric motors with precise sensors and immunized against stray fields that a solution is necessary: the inductive sensor. It is in this context that Melexis wants to position the company on the market of inductive position sensors.

In the world of angular position sensors, there are different technologies commonly used. The variable reluctance (VR) resolver is a position sensor solution widely used in traction motors. It is composed of a stator with several secondary coils and a ferromagnetic rotor. VR resolvers have long been used for position sensing of electrical machines and are very robust. But in Melexis, two other important types of angular sensors are developed, magnetic and inductive sensors. Both have their advantages and disadvantages depending on the application for which they are used.

A magnetic resolver uses the Hall effect for its measurements which makes it much more compact and less expensive than a variable reluctance resolver. These sensors avoid many disadvantages associated with optical devices, as they are less susceptible to foreign objects. However, these sensors are rarely used for high precision applications due to magnetic hysteresis and the need for precision mechanics between moving and stationary parts. Another consideration is the proximity of magnetic materials or electrical cables. Magnets can attract some foreign particles, and one source of failure is the gradual build-up of chips or particles.

Finally, an inductive resolver has the advantage of being immune to stray magnetic fields, very accurate over a wide speed range. Its design also makes it less expensive than the VR resolver. The comparison between these three technologies is summarized in the following table.

| Parameter / Technology             | VR            | Inductive      | Hall effect    |
|------------------------------------|---------------|----------------|----------------|
| Accuracy                           | high          | high           | medium         |
| RPM                                | high          | high           | medium         |
| Stray field immunity (ISO 11452-8) | yes           | yes            | limited        |
| System cost                        | high          | medium         | medium         |
| Output                             | analog        | analog/digital | analog/digital |
| Interface                          | additional IC | integrated     | integrated     |
| Size                               | medium        | medium         | small          |
| Weight                             | high          | medium         | low            |

Figure 1. Comparison of position sensing technologies

Several terms are used to characterize the performance of a sensor: The **accuracy** or the **linearity** are the difference between the output of the sensor and the actual position being measured.

The **precision** of a sensor refers to the measurement noise level and its degree of repeatability. The **resolution** of a sensor refers to the smallest increment or decrement of position that can be measured by it.

To select the right sensor for specific needs, it is not enough to take the one with the highest accuracy. Firstly, because it can be too expensive and secondly because high accuracy sensors require careful installation, which will not necessarily be possible due to the conditions of vibration, thermal dilation, and costs. Third, because some types of high precision sensors are also delicate and may experience malfunction or failure in harsh environments. It is therefore wiser to consider all the measurement conditions as well as the budget available to make a choice.

For some engineering applications, resolution and repeatability are more important criteria than linearity. In some machines accuracy and precision are key points. A position sensor offering high linearity, excellent resolution and high repeatability, even in wet and dirty conditions and with long maintenance-free periods, is therefore likely to be relevant.

In terms of price, magnetic sensors generally have a definite advantage as they are made from a semiconductor material and can therefore be integrated directly on a chip, reducing costs and size. PCB-free Hall effect magnetic sensors have also been developed, which allows them to be mounted directly on a platform using metal pins. Therefore, they are very suitable for applications which require placing sensors in small spaces. Inductive sensors are more competitive in terms of performance because they offer better precision, greater thermal robustness and total immunity to stray fields compared to magnetic sensors. However, inductive sensors with a range of 360 ° are strongly affected by mechanical misalignments which makes them more difficult to integrate. Another point to consider is that inductive sensors are limited to 2D detection where magnetic Hall sensors can be used to detect the position of the object in space (in 3D).

A large part of the sensors developed at Melexis are used in the automotive industry for electric motors. The main characteristic of the sensor must therefore be its reliability. Moreover, the pre-calibration error and the thermal drift are lower for the inductive sensor than for the Hall effect magnetic sensor. Also, the capacity of immunity to stray fields, that is to say the capacity of the inductive sensor to neglect external magnetic fields, is infinite, which has the effect of considerably increasing its reliability. Most of the information in this section come from Melexis.com [6].

Melexis is a technological innovation company created in Belgium and today established worldwide that designs, develops and supplies innovative micro-electronic solutions that allow designers to turn ideas into applications that change the future of technology. The developed integrated circuits communicate with the outside world by combining analog and digital signals. They improve safety, comfort, increase efficiency, and support durability.

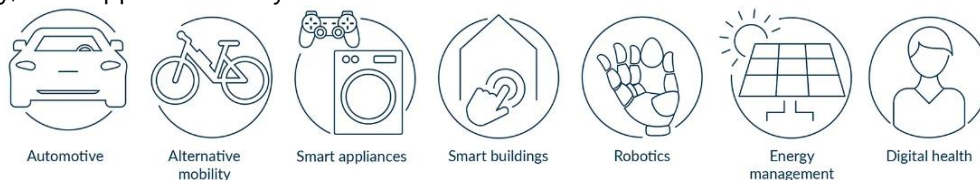


Figure 2. Main business sectors of Melexis

Melexis is one of the world leaders in automotive semiconductor sensors, and thanks to this experience, the company now also meets the needs of smart devices, home automation, industrial and health applications.

Now, Melexis has more than 1,700 employees spread over 19 sites and on 3 different continents.

The site on which my internship took place is based in Switzerland, in Bevaix, a small town of La Grande Béroche and a former Swiss municipality in the canton of Neuchâtel, located in the Littoral region. This is the magnetic sensor development center of Melexis, which also hosts an inductive pole.

During my internship, I was part of the Melexis inductive team, So I worked only with inductive sensors. The details of their design are explained in the following section.

## 2 Inductive sensors

### 2.1 General presentation

Melexis is currently developing inductive position sensors with two different integrated circuit architectures: the MLX90510 and MLX90517. Today, the MLX90510 sensor is the only one-induction position sensor solution to be marketed by Melexis. It will soon be followed by the MLX90517 which is a variant of this one. Let's start by describing the architecture and operation of an inductive position sensor as it is developed at Melexis. A large part of the information in this section come from Melexis.com [7] and from reference [4].

In a nutshell, an inductive position sensor is an accurate inductive high-speed resolver interface for brushless DC electric motors, permanent magnet synchronous motors, or other electrical machines that are used as traction motors or auxiliary motors for steering or braking. Its architecture allows it to minimize the motor control unit effort required to achieve good accuracy under extreme mechanical and electrical conditions.

The sensor allows working with an inductive transducer, processing the signals coming from the position of a metallic target which is placed in front of a set of inductive coils, and providing analog outputs (differential sine and cosine). A transmitter coil is coupled with three receiver coils and a target of which here is the overall diagram.

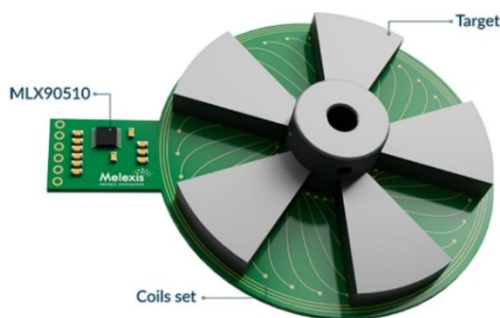


Figure 3. Melexis inductive sensor system

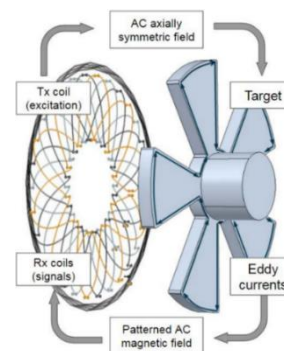


Figure 4. Inductive sensing principle for 5 pole pairs motor

With this sensor, to measure a position, a metal target is attached to the motor rotor. The target is composed of a certain number of branches which depends on the configuration of the receiving coils. This configuration depends on the number of poles pairs of the motor. These receive coils, in the center of the sensor, are called Rx. They are surrounded by a Tx transmission coil. These coils are integrated into the PCB which is attached to the motor stator, then they are connected to the rest of the integrated circuit.

Here is the general operation of the sensor described by Figure 4:

First, the transmission coil is powered by the integrated circuit of the sensor to produce an AC magnetic field. If a target is above the sensor, depending on its position at time  $t$ , it allows the magnetic field to be reflected on it in the direction of the receiving coils. This reflected field is picked up by the three-phase Rx coils, in which three alternating signals are generated.

Secondly, the integrated circuit of the inductive sensor receives these AC signals and converts them into differential signals (sin+, sin-, cos+ and cos-) which are the output signals. These latter signals are communicated to the engine control unit (ECU that recovers the angle via an arctan calculation).

## 2.2 Working principle of inductive position sensors

Inductive position sensors are based on Faraday's law: a circuit subjected to a variable magnetic flux  $\phi$  (resulting from a variable magnetic field  $\mathbf{B}$ ) undergoes an electromotive force  $\epsilon$ .

$$\epsilon = - \frac{d\phi}{dt}$$

They have an excellent reputation for their safety and reliability in harsh conditions, making them an almost automatic choice in many safety-related applications.

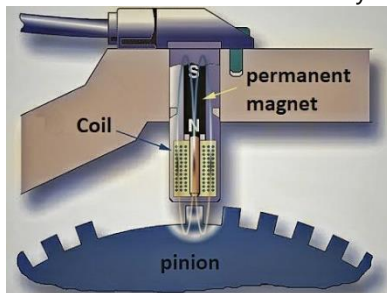


Figure 6. Inductive speed sensor principle



Figure 5. Inductive absolute position sensor principle

Older generation inductive sensors are basically variable reluctance resolvers. These are passive sensors. They consist of a magnet and a winding around this polar part. The passage of a ferrous element generates a voltage across the winding. The voltage varies according to the speed of rotation of a gear (pinions) or holes machined in a flange. This variation is then converted by an acquisition system to deduce the speed.

But today, a new generation of inductive sensors is used in the industrial manufacturing, automotive, or also medical equipment markets. These inductive sensors use the same basic physics as traditional devices, but they use coils made of copper, printed circuit and digital electronics, instead of transformers and other bulky analog components. This approach is elegant and broadens the range of applications for inductive sensors. This measurement method allows high performance in a cheaper device.

## 2.3 The four parts of the inductive sensor

An inductive resolver can logically be divided into four distinct parts: coils, target, integrated circuit (IC) and PCB.

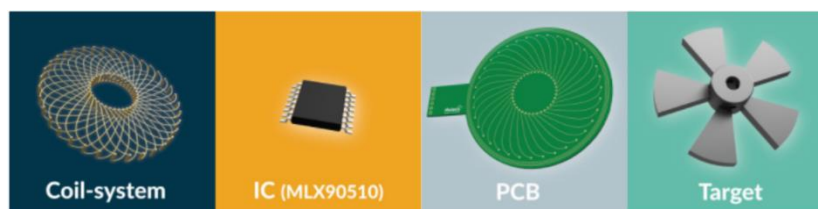


Figure 7. The four parts of an inductive sensor

### 2.3.1 Coil-system and PCB

The Coils can be considered as the transducer of the whole system. They can be designed in different ways. The chip is designed independent of the transducer and can adapt to different configurations. It is the number of motor pole pairs and the needs of the application which will determine the periodicity of the coils. Different periodicities are explained below, this adaptability makes it possible to be consistent with the electrical period of the motor. Theoretically, the maximum number of sensor periods supported can be infinite, but certain physical and industrial constraints limit this number.

The more pair poles an electric motor has, the more torque it can deliver. However, a large number of pair poles will limit its maximum speed. In an electric car, motors generally have between three and six pair poles. Sensors with a single pair pole are not directly used to control the motor. They are generally used in small systems (windows, valves, seat) which use small motors, to know the value of a single displacement. These are applications in which it is also possible to use magnetic sensors but which are not immune to external magnetic fields.

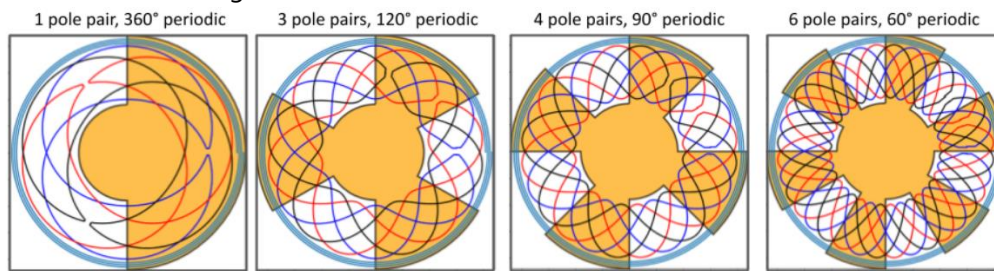


Figure 8. Examples of different pair poles configuration

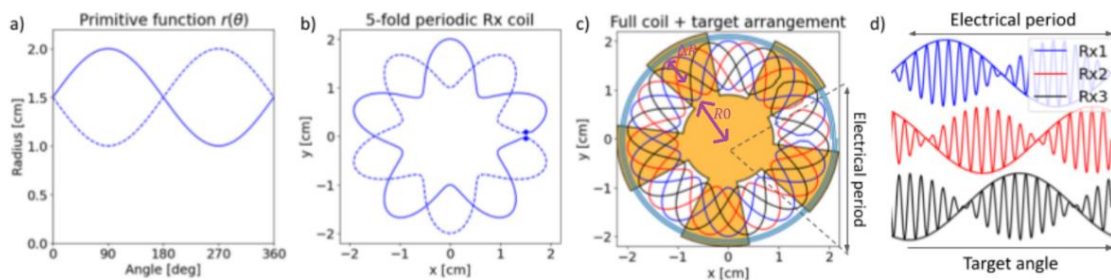


Figure 9. Coil design for 5 poles pairs

Let's describe the design of receive coils using the following example: A transducer matched to  $N = 5$  pole pairs and dimensional constants  $\Delta R$  and  $R_0$

A sinusoidal primitive function and its complement are used to define the initial shape of the coils:  $r(\theta) = R_0 + \Delta R \sin(\theta)$  and  $r'(\theta) = R_0 - \Delta R \sin(\theta)$ . With a transformation in polar coordinates we obtain the final pattern of an Rx Coil. Here the transformation is adapted to the constraint of having five periods on a mechanical turn.

$$\begin{aligned} x &= r(N\theta) * \cos(\theta) \\ y &= r(N\theta) * \sin(\theta) \end{aligned}$$

To obtain the two other Rx coils, simply repeat the operation shifting by  $120^\circ/N$ . Finally, the Tx coil is added around the reception coils. A target with  $N$  pairs of poles makes it possible to obtain the signals of Figure 9 d).

The angular signal from the sensors, which give a cosine and sine value at the output, do not correspond to a complete revolution of the target on itself, but to a revolution divided by the number of poles of the target, it is then question of electrical angle, and mechanical angle.

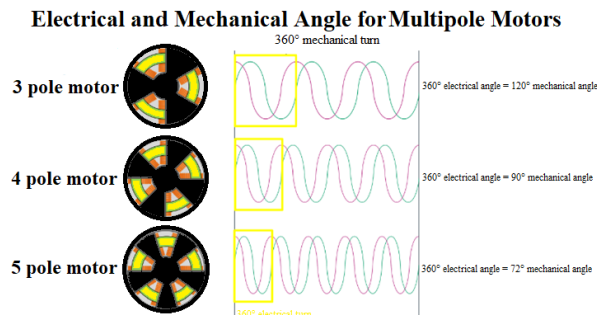


Figure 10. Electrical and Mechanical Angle for Multipole Motors

The PCB technology used must be cost effective. The plate must be adapted to the via dimensions, thick enough to have adequate mechanical strength, to be compatible with harsh environments and a certain temperature range, and to be composed of a maximum of four layers.

### 2.3.2 Target

In application, the target is fixed to a rotor and its design is adapted to the number of poles of the motor. The target must be a piece of metal (aluminum, steel) and of sufficient thickness for a good mechanical rigidity but which has no influence on the signal. The power supply creates a current in the Tx coil which induces eddy currents in the target, generating a magnetic field which will also create a current in the Rx coils.

When, as described by Faraday's law, there is a varying magnetic field in a conductive material, closed loops of electric current are created in that conductor and perpendicular to the magnetic field. These loops are called eddy currents. These currents are illustrated below.

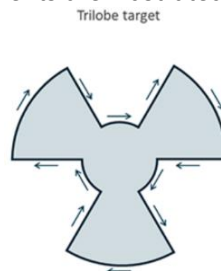


Figure 11. Eddy currents in a target

### 2.3.3 Integrated Circuit

The integrated circuit of the inductive sensor excites the transmission coils, which creates the eddy currents in the target. It then generates a voltage in the 3 coils and finally processes these 3 voltages. This signal processing is, for the MLX90510, composed of several parts (Figure 12): The signal is filtered (EMC Filter), amplified (Tri-Amplifier), demodulated (Baseband conversion, Multiplexer), and digitalized (go through a digital signal processor or DSP unit). There is common mode suppression, offset compensation, digital angle calculation, linearization and propagation delay compensation. After all these modifications, the signal is transferred to the ECU in the form of sine and cosine.

The figure below summarizes the electronic circuit required to perform signal analysis, associated with the MLX90510 resolver. Here the sin and cos signals are reconstructed.

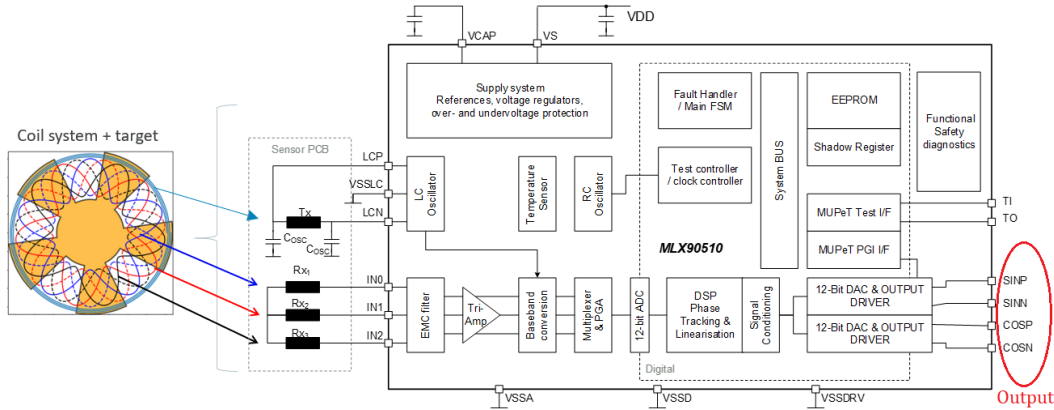


Figure 12. IC schematic of MLX90510

It is here that we can notice the real difference between the MLX90510 and the MLX 90517. They are identical at the level of the coils, the targets used, the PCB but differ in their way of processing the input signals from the Rx coils. In their current form, the integrated circuit of the MLX90517 is physically identical to that of the MLX90510, but a part of the digital section is bypassed. Signal processing is limited to an offset pre-compensation and a Clarke's transformation. The signals found at the output of the MLX90517 are analog but "raw", in the sense that they are simply obtained by performing a Clarke's transformation on the three digitalized input signals. The output signals are thus representative of to the signals in the Rx coils (signals named IN0, IN1 and IN2), and their amplitude depends on the strength of the signal, which is not the case for the MLX90510.

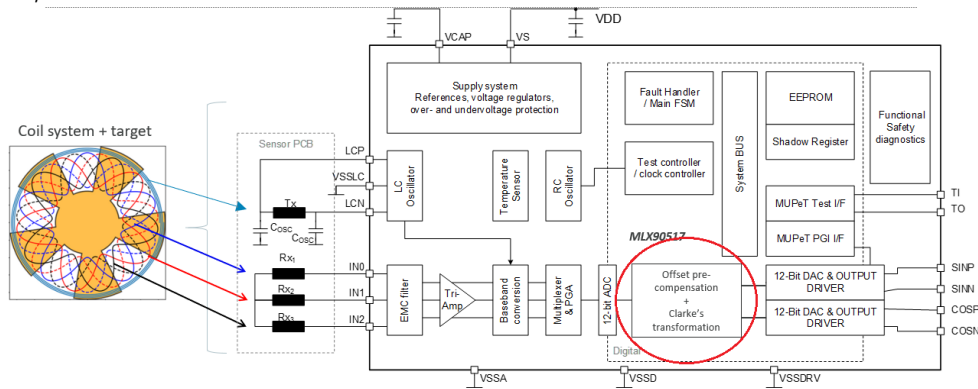


Figure 13. IC schematic of MLX90517

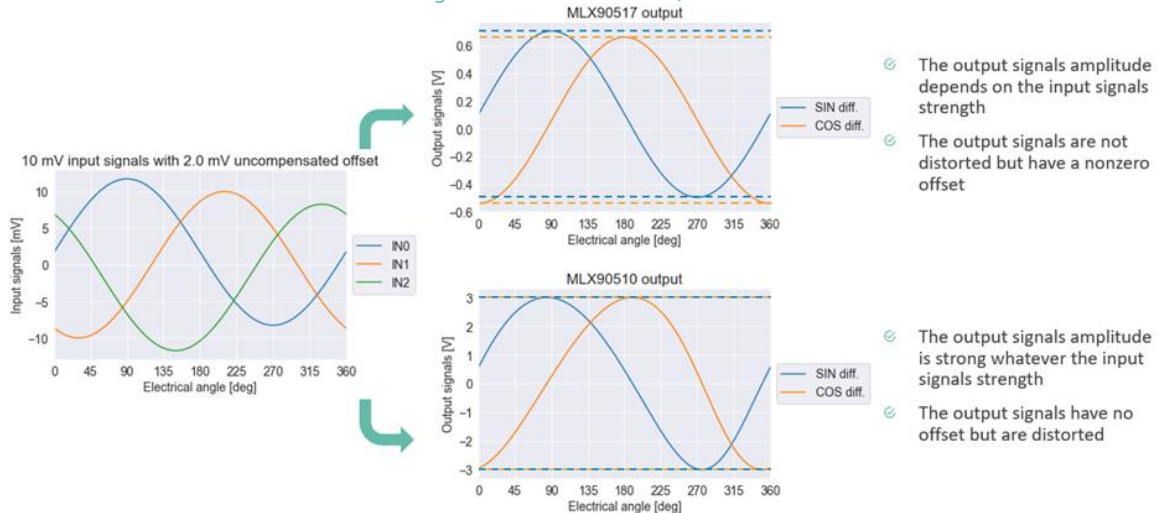


Figure 14. Signal MLX90510 vs MLX90517

The main difference of the MLX90517 versus the MLX90510 is that its output signals can be post-processed in the Electronic Control Unit (ECU), an on-board computer or system that controls physical devices within a machine in the automotive field, while this is not possible with the MLX90510. For example, Figure 14 shows how an offset not directly compensated within the IC would result in different output signals when using the MLX90510 or MLX90517. In the case of the MLX90510, the signals with uncompensated offset are used to calculate an angle from which the output Sine/Cosine signals are synthesized. This results in output signals with a distorted shape which can't be easily corrected by the ECU. The MLX90517, on the other hand, outputs two signals with perfect sinusoidal shape but still carrying an offset, which can be easily tracked and corrected by the ECU. The MLX90517 mode of operation is found a lot among Melexis competitors. There is therefore a certain demand on the market for this type of sensor. The MLX90517 approach has however some disadvantages. For example, the strength of its output signals depends directly on the input signals strength and the selected IC gain, while the MLX90510 outputs signals with fixed and large strength. Furthermore, in the MLX90517 the propagation delay is not compensated as in the MLX90510, which induces measurement errors at high speeds.

Melexis started developing the MLX90517, in part because some customers want to buy a sensor that outputs the raw data from the receive coils. On the one hand because it is possible to work on this data and because these customers believe they can obtain better performance from it than with the MLX90510. Some also do not want to use the interfaces developed by Melexis (Ptc04) to calibrate the sensors to save time and efficiency. One of the main questions that we want to answer here, for different sensor configuration, is: Is it relevant to always use a MLX90517 instead of a MLX90510?

## 2.4 Inductive sensing modes

The whole system can be arranged in different mounting positions depending on the needs of the application. Three different positions on the shaft are possible:

End of Shaft (robust to mechanical tolerances, small size, low cost), Through Shaft (strength to mechanical tolerances, medium size, medium cost), Side of Shaft (sensitive to mechanical tolerances, small size to large diameter, low cost)



Figure 15. Sensor position configuration

End of shaft is the preferred configuration to use when it's possible to access to the end of the shaft. When it's not possible because of the motor design, a through shaft design is used. This design works very well but generates additional costs due to its larger dimension, and its large need of plastic. In this case, the side of shaft design is a great solution to reduce costs.

This sensor has a wide range of application for electric vehicles. It is effective to determine the angular position of the rotor of a traction motor, to control braking systems, valves or even power steering as shown in Figure 16

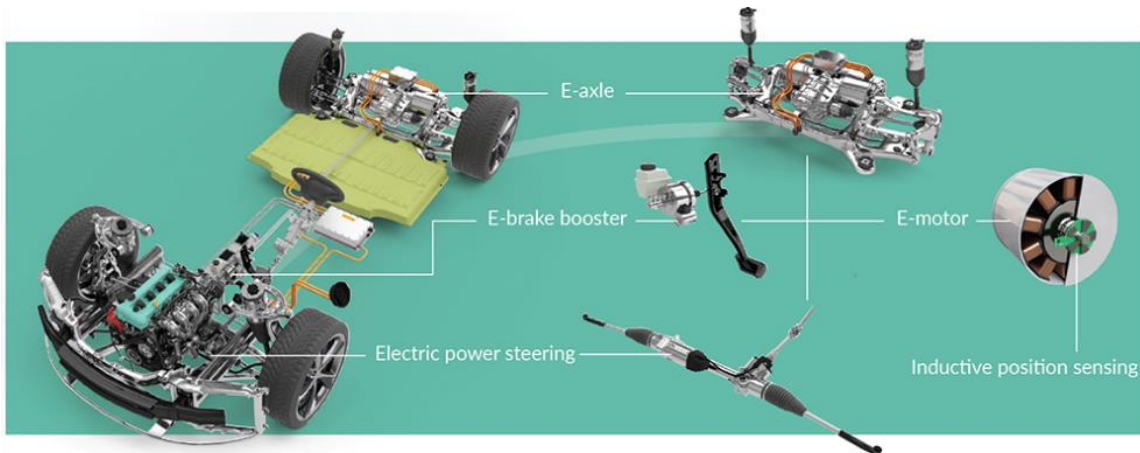


Figure 16. MLX90510 applications

## 2.5 Error source of inductive sensors

Although it can be very accurate, the inductive sensor still suffers from slight measurement errors. These errors are mainly related to certain influencing parameters.

On one hand there is some fixed geometrical parameters, determined by how the sensor and target are designed (sensor inner radius being the minimal distance between the center of the sensor and the closest Rx coil and the sensor outer radius being the maximal distance between the center of the sensor and the furthest Rx coil, vertical distance between coils, inner and outer radius of target etc..).

On another hand, for each sensor there is an offset error that must be eliminated. This offset comes partly from the direct coupling between the Tx and Rx coils. But for each measurement setup, the environment in which the sensor is placed can be a source of offsets. There may be pieces of metal close to the coils or metal structures surrounding the sensor that can affect the signal. One of the big steps in setting up a sensor is to eliminate these offsets.

During my tests, I am comparing the behavior of uncalibrated and calibrated sensors. Let us specify what type of calibration it is. It is a DC-Offset compensation carried out with a PTC04 (automated in it). This is one of the methods used to reduce the angular error. In my measurements, for some technical reasons (I could not run the motor at a given constant speed without break), I used the DC offset calibration without the target. This procedure can be found in a Melexis application note [5].

This calibration method is limited because the target must be removed. This is not possible in some industrial cases and the target can be an offset source that this method cannot detect and compensate. This method is, in general, not recommended but give a great idea of the behaviour of a calibrated sensor. A calibrated sensor with rotor is a little more precise but its behaviour does not change completely.

Let's explain how a calibration procedure works. To simplify, we start by studying the case of a perfect sensor. The received signals ( $IN_0$ ,  $IN_1$  and  $IN_2$ , the three signals of the three receiving coils) envelopes should only depend on the target angle in a sinusoidal way and these receiving coils should not generate a signal in the absence of a target. The three signal envelopes are, one with respect to the other, shifted by  $120^\circ$ :

$$IN_0 = \frac{1}{\sqrt{3}} A_{rotor} \sin\left(\varphi - \frac{1}{6}\pi\right), \quad IN_1 = \frac{1}{\sqrt{3}} A_{rotor} \sin\left(\varphi - \frac{5}{6}\pi\right), \quad IN_2 = \frac{1}{\sqrt{3}} A_{rotor} \sin\left(\varphi - \frac{9}{6}\pi\right)$$

With  $\varphi$ , the electrical angle.

However, this is a purely theoretical view. In practice the behaviour of the coils is different. There are imperfections in the coil geometry such as coil side terminations in C-shaped geometries or feeding wires, there may also be some mismatches in the IC. In real use, even in the absence of the target, a signal is generated. With a target, the signal generated by the receiving coils will contain a DC component generated on one side by the target in function of the airgap (The closer the target is to the sensor, the stronger this offset is) and on the other by these spurious and unwanted effects.

Therefore, the three signal envelopes are, in a more realistic view, described by these equations:

$$IN_0 = \frac{1}{\sqrt{3}}A_{rotor} \sin\left(\varphi - \frac{1}{6}\pi\right) + A_{common} + A_{asym0}, \quad IN_1 = \frac{1}{\sqrt{3}}A_{rotor} \sin\left(\varphi - \frac{5}{6}\pi\right) + A_{common} + A_{asym1},$$

$$IN_2 = \frac{1}{\sqrt{3}}A_{rotor} \sin\left(\varphi - \frac{9}{6}\pi\right) + A_{common} + A_{asym2}$$

With the common part of the DC spurious signals ( $A_{common}$ ) and a coil specific component ( $A_{sym}$ ).

These signals are differentially amplified in pairs through the triamplifier, synchronous rectification and low pass filtering. This results in three baseband signals modelled as follows:

$$D01_a = IN_0 - IN_1 = A_{rotor} \sin(\varphi) + A_{asym0} + A_{asym1}, \quad D01_a = IN_0 - IN_1 = A_{rotor} \sin(\varphi) + A_{asym0} - A_{asym1}$$

$$D12_a = IN_1 - IN_2 = A_{rotor} \sin\left(\varphi - \frac{2}{3}\pi\right) + A_{asym1} - A_{asym2}, \quad D20_a = IN_2 - IN_0 = A_{rotor} \sin\left(\varphi - \frac{4}{3}\pi\right) + A_{asym2} - A_{asym0}$$

The calibration is actually a PCB offset compensation which aims to compensate for the DC offsets of the D01a, D12a and D20a signals induced by  $A_{asym0}$ ,  $A_{asym1}$  and  $A_{asym2}$  to finally obtain the offset-free baseband signals which can be used for the angle calculation.

$$D01 = IN_0 - IN_1 = A_{rotor} \sin(\varphi), \quad D12 = IN_1 - IN_2 = A_{rotor} \sin\left(\varphi - \frac{2}{3}\pi\right), \quad D20 = IN_2 - IN_0 = A_{rotor} \sin\left(\varphi - \frac{4}{3}\pi\right)$$

On a last hand, there are certain variable parameters which are more difficult to control like the air gap and some mechanical tolerances.

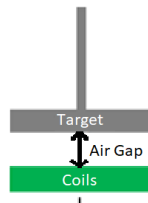


Figure 17. Air gap illustration

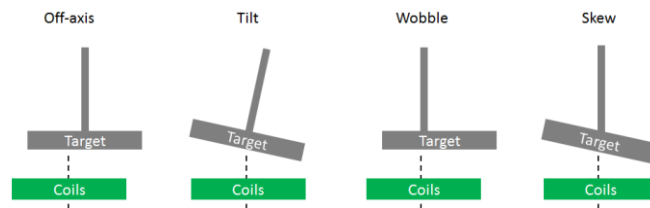


Figure 18. Four types of mechanical tolerances

The air gap is defined by the distance between the PCB, where the coils are, and the target surface. This parameter is directly linked to  $A_{rotor}$  [mV], the quantity that quantifies the strength of the signal. The closer the target is to the PCB, the lower is the air gap, the higher is  $A_{rotor}$  and better is the signal quality. Obviously, the target, to rotate, can't come in contact with the PCB.

The mechanical tolerances do not affect the signal strength but create some angular error. These tolerances can be divided into four types: An off axis describes a situation in which there is a misalignment between the axis of rotation of the target and the axis of the coils (the axis perpendicular to the plane parallel to the coils, and in the center of the coils). These two axes are shifted horizontally with respect to the plane parallel to the coils. The off axis is described by a magnitude and a direction on a plane. A tilt describes a situation in which the axis of rotation of the target describes a non-zero angle with respect to the normal to the plane of the coils (parallel to the coils). The tilt is described by an inclination and an azimuth. There is a Wobble when the center of the target is misaligned with the axis of rotation of the target. The Wobble is described by a magnitude and a direction. There is a Skew if the axis of rotation of the target is perpendicular to the plane of the coils but not with the plane of the target. Like the tilt, the skew is described by an inclination and an azimuth.

With the Melexis lab setup, only off axis and tilt are controllable. Wobble and Skew are problems that we have to deal with during the measurements. In addition, it can be proved that wobble and skew are respectively just special type of tilt and off axis. All measurements and simulations in this report will focus on three variables: air gap, tilt, and off axis.

### 3 Project goal and timeline

#### 3.1 Project goal

Accuracy is one of the most important features of an inductive sensor, influenced by several factors (sensor geometry, mechanical tolerances, IC signal chain, etc.). The two different interface ICs for inductive motor position sensing proposed by Melexis have each their own strengths and weaknesses but an overall study of the accuracy of these two different inductive sensors topologies coupled with different ICs has not yet been performed within Melexis.

In this context, the purpose of the project is to perform a full-blown analysis of the accuracy of inductive position sensors, study and compare the MLX90510 and the MLX90517 interface IC for position measurement in different topologies (number of poles, O or C\_shape) and also propose different algorithms to improve performance of each approach. A subsidiary objective is to compare the performances and behaviours of the selected sensors in simulation and in measurement.

#### 3.2 Project Timeline (The internship starts week 7 of 2022)

Here is the initial schedule for this internship.

| WORK PACKAGE  | DESCRIPTION  |
|---|--|
| WP1: Simulation and evaluation of different inductive sensors → target end Week 12<br>(from February 14 <sup>th</sup> to March 24 <sup>th</sup> )   | <ul style="list-style-type: none"> <li>Simulation of various inductive sensor, O-shaped 5PP, C-shaped 5PP and O-shaped 1PP, 10mm</li> <li>Provide report describing performance of each sensor (inductance, signal strength, offsets, intrinsic nonlinearity, sensitivity to misalignments)</li> </ul>   |
| WP2: experimental setup → target end Week 16<br>(from March 24 <sup>th</sup> to April 21 <sup>st</sup> )  | <ul style="list-style-type: none"> <li>Experimental measurements with low and high-speed setups, with MLX90510 and MLX90517</li> <li>Accuracy measurements,</li> </ul>   |
| WP3: quantification of offset/gain and orthogonality mismatch between MLX90510 and MLX90517 and output noise → target end Week 20<br>(from April 21 <sup>st</sup> to May 19 <sup>th</sup> ) | <ul style="list-style-type: none"> <li>Offset, amplitude and orthogonality should be quantified for each sensor at input and output of the IC</li> <li>Describe the impact of mechanical tolerance introduced on each sensor</li> <li>Evaluate the effectiveness of output signal postprocessing (offset corrections etc.) for error mitigation</li> <li>Quantification of noise at output in static, with different offsets and mechanical tolerances, present in both sensors</li> </ul> |
| WP4: Evaluation of a two-coil system approach, and effect of mechanical tolerances → target end Week 24<br>(from May 19 <sup>th</sup> to June 16 <sup>th</sup> )                            | <ul style="list-style-type: none"> <li>Evaluate offset and gain mismatch for 2 coils system</li> <li>Evaluate calibration algorithm that are needed to reduce offset/gain mismatch and orthogonality error.</li> </ul>   |
| WP5: detailed report and conclusion showing advantage and drawback of each solution → target week 28<br>(from June 16 <sup>th</sup> to July 14 <sup>th</sup> )                              | <ul style="list-style-type: none"> <li>Report and conclusion on different sensors</li> </ul>   |
| WP6: work on remaining issues, and rewrite parts of the report<br>(from July 14 <sup>th</sup> to August 12 <sup>nd</sup> )  |  |

Table 1. Project timeline

## 4 Coil design and simulation

### 4.1 O-shaped and C-shaped inductive position sensors: theory of coil design

Inductive sensors can be divided in three families: O-shaped coils, C-shaped coils and linear coils.

**O-shaped coils:** It is the most accurate type of Coil for detecting the position of a motor. They are found in end-of-shaft or through-shaft electric motor position sensing applications, as well as in other end-of-shaft applications such as throttle valves or accelerator pedals.

**C-shaped coils:** This type of coil is less precise than the previous one but also more affordable in terms of cost because a shorter winding is necessary. They are used in shaft side mode motor position sensing applications. These sensors are more sensitive to mechanical tolerances.

**Linear coils:** This type of coil is logically useful for detecting linear variations in position.



Figure 20. C\_shaped PCB



Figure 19. O\_shaped PCB

Finally, a C-shaped has the only advantages of being cheaper and less cumbersome compared to an O-shaped but is less accurate.

During my work, I worked with O and C type of sensor shapes, because according to certain situations, their behaviour differs in an interesting way.

To design a sensor, and to simulate its physical behavior, one of the important parts to take into account is the coil system.

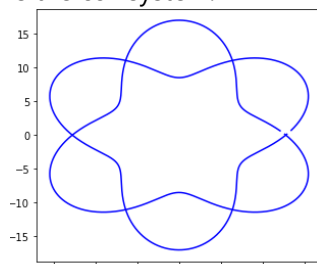


Figure 21. 2D coil path

For this purpose I participated in the development of a program written in python, which creates a 3D winding model from initial characteristics that we want to associate with the sensor (size, number of poles, thickness etc.). In this example it is an O\_shape.

By reusing the formulas of the previous part (under figure 16), one can easily construct the path of the coils in 2D as shown in figure 22.

To reform the path of the coils in 3D it is necessary to follow certain construction steps:

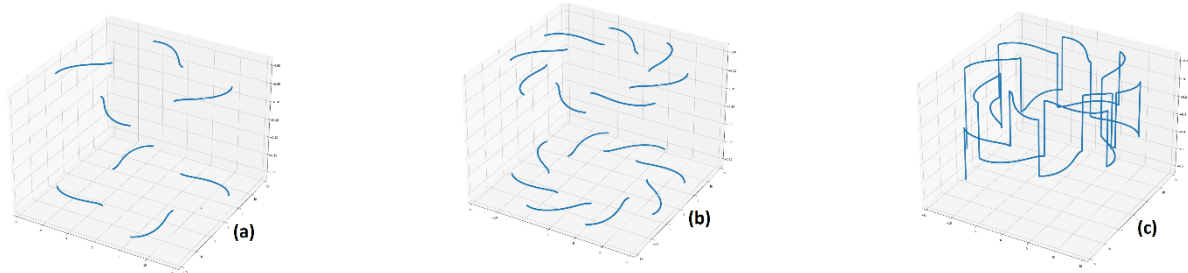


Figure 22. 3D coil path construction part one

It is first necessary to place the first wires in an arc of a circle on two planes (a), It is then possible to place the complementary wires (b), and finally to connect the planes to each other as well as to correctly close the path (c)

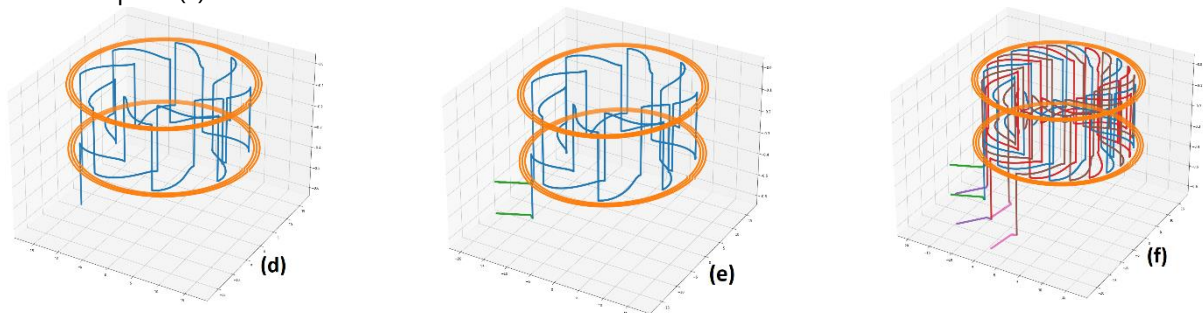


Figure 23. 3D coil path construction part two

It is then necessary to add the Tx coils (d), place the connections (e), and then finally to build the two other Rx coils by shifting 120 degrees, divided by the number of poles (f). Now we have a 3D model for the coil path of the inductive sensor to be designed.

## 4.2 Working principle

To work on a sensor, the first step is to design it on Altium. It's an electronic CAD (computer-aided design) to design PCB, with which one can obtain diagrams similar to the following and transferable files to Comsol for physical simulations. I did not participate in this part of the work which was done by the engineers of the inductive team. After this step, each sensor is simulated with Comsol.

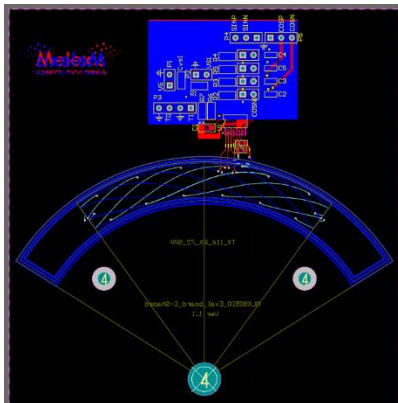


Figure 24. Altium Design of 5PP C\_shape

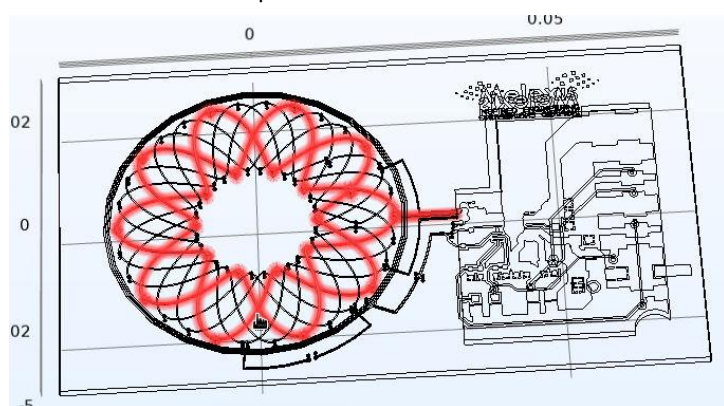


Figure 25. Importation of the O\_shaped 5PP model with an Rx\_Coil

For the simulation to work there is some work to do (remove some parts, merge others, etc.) The main goal is to simulate the interactions between the coils and the target. The results are compiled into csv files which are then analyzed with a python script.

The simulation provides this type of data:

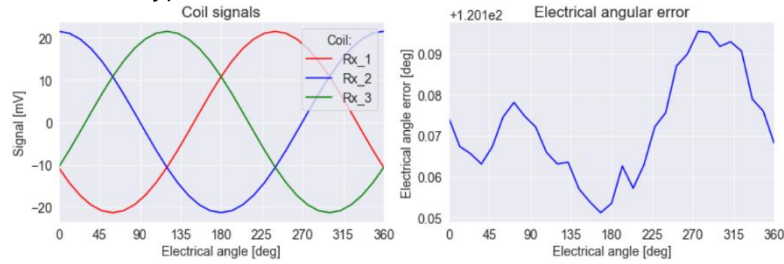


Figure 26. Rx coil signal and error for an O-shaped 5PP at nominal position

The signal of the receiving coils is measured on a mechanical turn, which allows, with certain formulas, by comparing it with the expected signal to extract the measurement error. Other data can be extracted from these curves as we will see in the following sections.

The 3 signals of the receiver coils are named Rx\_1 (or IN0) , Rx\_2 (or IN1) and Rx\_3 (or IN2). Then, 4 quantities that will help to calculate some important values are created: CALRESAOC, CALRES01, CALRES12 and CALRES20.

CALRESAOC is the measured average oscillator (LCO) amplitude. CALRES01, CALRES12 and CALRES20 are the measured average baseband DC offset for difference of inputs IN0 and IN1 (channel D01), inputs IN1 and IN2 (channel D12) and inputs IN2 and IN0 (channel D20).

They are defined like that:

IN0 = (CALRES01- CALRES20), (IN0 after common mode and offset removal in mV)

IN1 = (CALRES12- CALRES01), IN2 = (CALRES20- CALRES12)

With these formulas, it's possible to obtain the signal strength, the sine and cosine of the phase:

$$A_{rotor} = \sqrt{\frac{(IN0^2 + IN1^2 + IN2^2)2}{3}}, \quad Sin = CALRES01, \quad Cos = \frac{CALRES20 - CALRES12}{\sqrt{3}}$$

With these formulas, it is possible to reconstruct all the necessary information. The phase is obtained with the arctangent of sin and cos, phase that is compared to the expected signal (real position of the target) to obtain the measurement error. Then, when we want to compare several errors, it is possible to subtract the error considered as initial from all the others to better understand the differences.

The programmed differential offset compensation is made with three values: DC01, DC12 and DC20, the user must determine these values (with an algorithm) to have a satisfying calibration.

These values are then added to the signal like this:

IN\_compensated = IN - DC\*CALRESAOC for each IN signal.

### 4.3 O-shaped 5PP simulation results

Here, in Figure 27, is the 3D model on which the simulations were performed. This sensor has an external diameter of 54 mm. The simulation procedure aims to focus on three measures: The signal strength, the On-axis accuracy, and the quantification of the  $\zeta$  parameter.

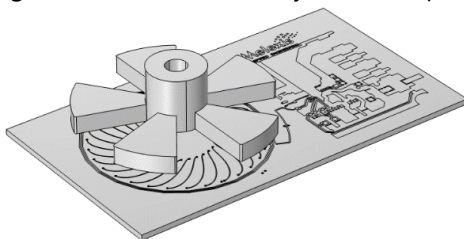


Figure 27. Simulation model O-shaped 5PP

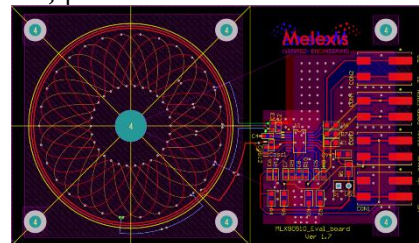
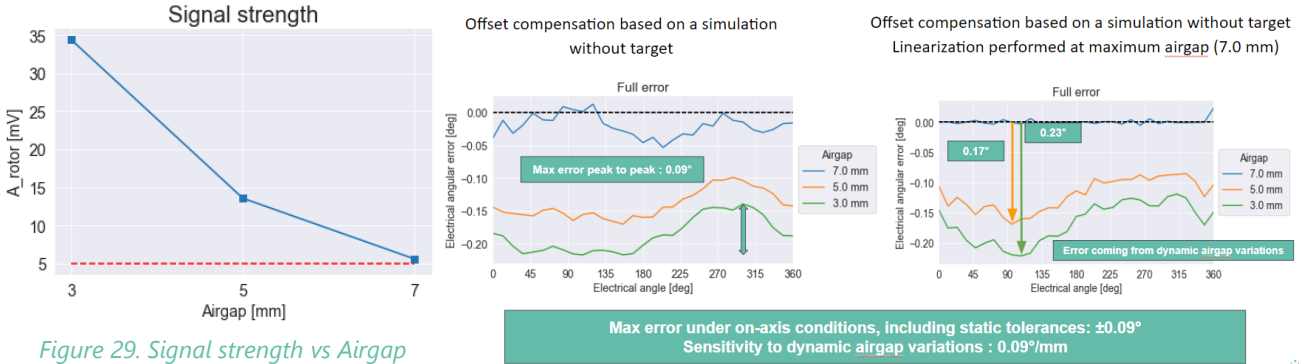


Figure 28. O-shaped 5PP Altium layout

Above you can see the 3D model of the sensor and its target as presented in Comsol Multiphysics software and its layout designed with Altium.



The signal strength curve decreases exponentially with air gap, which limits its maximum value to 7 mm (Arotor > 5 mV). Mechanical tolerances are presented as follows:

For the error on axis, we note that a simple offset compensation is already sufficient to have excellent results. This compensation is obtained by making a measurement without target.

The linearization is not very useful for an Oshaped with a number of poles greater than two because on axis error is already very low before linearization.

The  $\zeta$  parameter is useful to quantify the influence of mechanical tolerances on the measurement error of the sensor. The formula which describes the evolution of the angular error as a function of the

$$\varepsilon = \zeta \cdot [OA_x \cdot T_y - OA_y \cdot T_x + W_x \cdot S_y - W_y \cdot S_x + (OA_x \cdot S_y + W_x \cdot T_y - OA_y \cdot S_x - W_y \cdot T_x) \cdot \cos(\alpha) + (OA_x \cdot S_x - W_y \cdot T_y + OA_y \cdot S_y - W_x \cdot T_x) \cdot \sin(\alpha)]$$

Equation 1. Multipoles O\_shape Error equation

Let us describe the parameters of this equation.  $\alpha$  is the mechanical (NOT the electrical) angle,  $\zeta$  is not dependent on the mechanical tolerances,  $OA_x$  is the off-axis in the x direction,  $OA_x = OA_m \cdot \cos(OA_d)$   $OA_y$  is the off-axis in the y direction,  $OA_y = OA_m \cdot \sin(OA_d)$ ,  $T_x$  is the tilt in the x direction,  $T_x = T_i \cdot \cos(T_a)$ ,  $T_y$  is the tilt in the y direction,  $T_y = T_i \cdot \sin(T_a)$ ,  $W_x$  is the wobble in the x direction,  $W_y$  is the wobble in the y direction,  $S_x$  is the skew in the x direction,  $S_y$  is the skew in the y direction,  $\varepsilon$  is the angular error.

All parameters of this formula are known, except the zeta parameter  $\zeta$ .

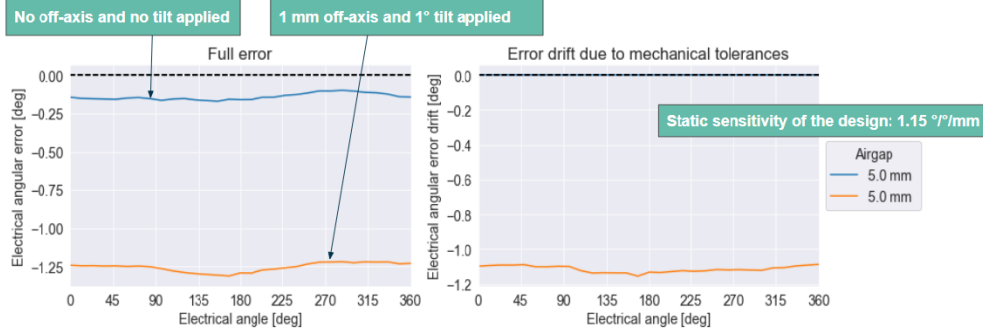
Off-axis and tilt alone generate constant errors. Therefore, the effect of static tilt and off-axis is negligible as this constant error is easily corrected.

Only a static tilt coupled with a dynamic off-axis or a static off-axis coupled with a dynamic tilt can generate a contribution to the error budget.

Tilt coupled with wobble or off-axis coupled with skew introduce errors which are periodic over a full mechanical turn and which thus contribute to the error budget.

For an angular position sensor, the residual mechanical tolerances (or misalignments in nominal position) can be quantify with this equation. However, it is necessary to use a measurement setup capable of controlling each quantity independently and in a controlled way (like the hexapod from the Melexis laboratory).

In the simulation, there is no skew or wobble so it's easy to obtain  $\zeta$  by applying a y-tilt and a x-off axis:  $\epsilon = \zeta[OA_x \cdot T]$ . And there are the results:



Error introduced by 1 mm x-off-axis and 1.0° y-tilt (no skew or wobble in this simulation): 1.15°.

This means  $\zeta = 1.15 \text{ } ^\circ/\text{mm}$ .

Figure 31. Quantification of the  $\zeta$  parameter O\_shaped 5PP

Here the error at the nominal position is compared with the error corresponding to an x-tilt of 1° and a y-off-axis of 1mm. The first error curve is subtracted from the second in order to best estimate the deviation. it is 1.15° which corresponds to the value of  $\zeta$ .

#### 4.4 O-shaped 1PP simulation results

Here is the 3D model on which the simulations were performed.

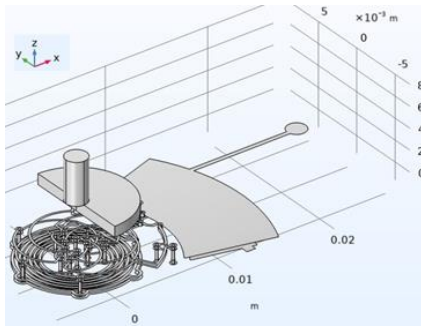


Figure 33. Simulation model O\_shaped 1PP

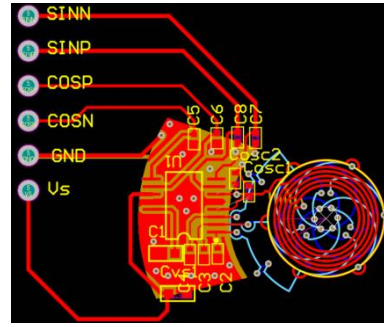


Figure 32. O\_shaped 1PP Altium layout

Above you can see the 3D model of the sensor and its target as presented in Comsol and its layout designed with Altium. This sensor is much smaller than the previous one, with an external diameter of 10 mm.

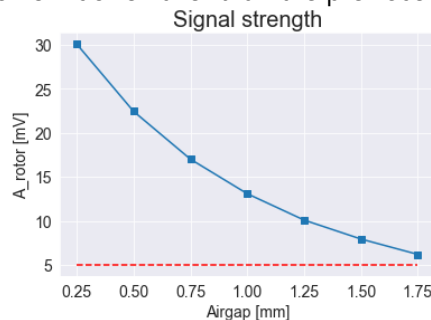


Figure 34. Signal strength vs Airgap O\_shaped 1PP

The signal strength curve has the same shape (decrease exponentially) but the target and the sensor must be much closer to each other to have a signal of adequate strength. With an air gap of more than 1.75 mm, it is considered that the sensor is no longer in its optimal operating zone (Arotor < 5mV). It was more than 7 mm for the previous one.

As for the O\_shaped 5PP, an on-axis accuracy measurement was made.

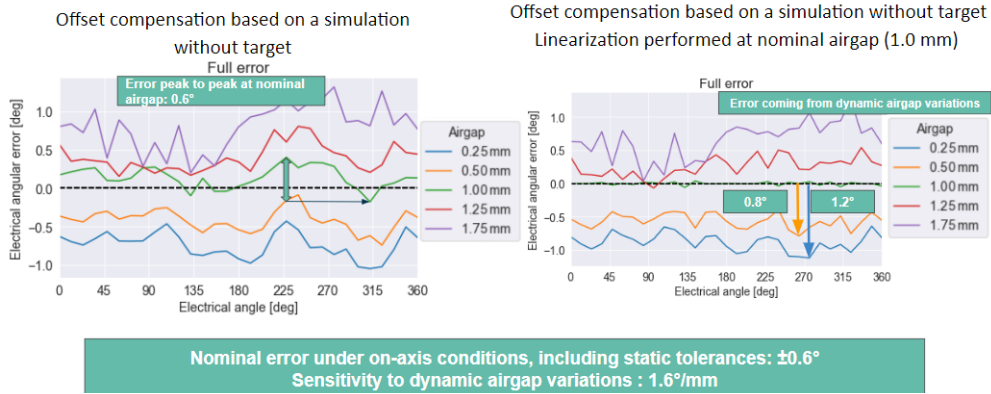


Figure 35. On-axis accuracy O\_shaped 1PP

We realize that because of its small size and its much simpler design, this sensor is much less accurate than the previous one. The error under nominal conditions with calibration is about 7 times greater than the 5-pole pair sensor, and it is 10 times more sensitive to air gap variations. For this case, the linearization is much more efficient.

Because of its simpler design, the calculation of  $\zeta$  is not done as before. Here the off-axis and the tilt each have a distinct contribution to the error that is relevant to measure.

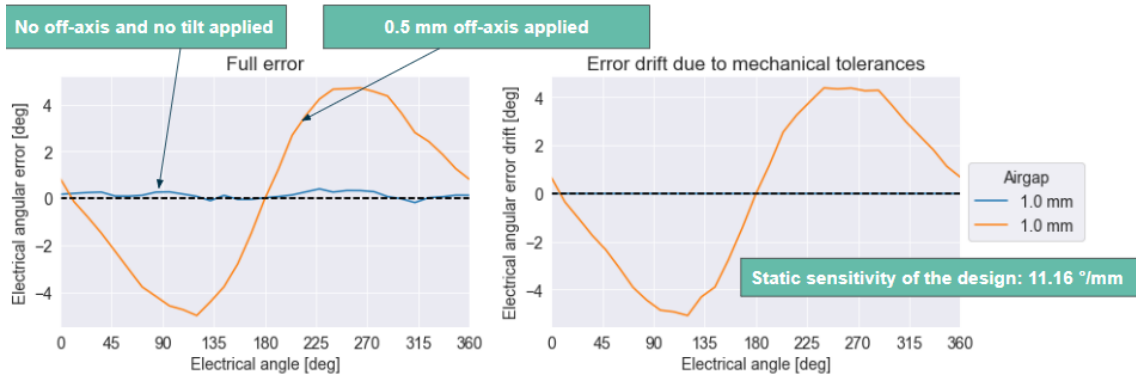


Figure 37. Quantification of the off-axis contribution for a O\_shaped 1PP

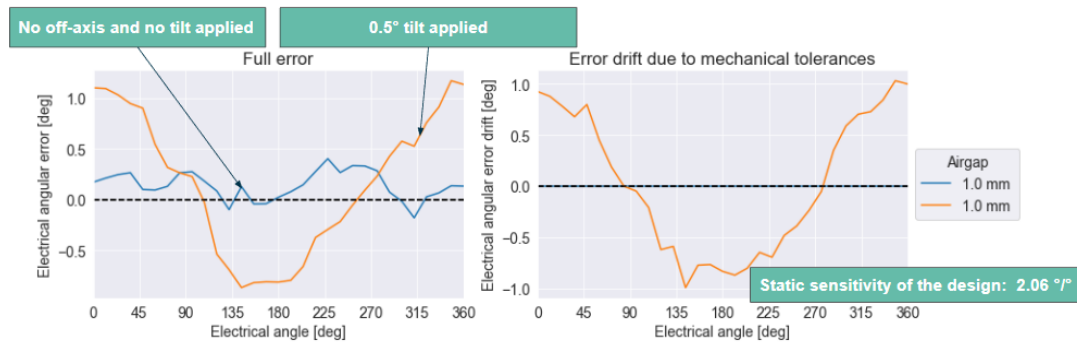


Figure 36. Quantification of the tilt contribution for a O\_shaped 1PP

To obtain these curves, the nominal error curve is subtracted from the one corresponding to a tilt or an off axis. The curves obtained are quite close to sinusoidal curves.

There is in fact a fundamental difference between an O\_shaped 5PP and an O\_shaped 1PP. In a sensor, at individual electric periods level, there is an individual contribution of off axis and tilt to the error. This

is a first order contribution. However, if the sensor contains more than one electrical period and a complete coil turn (O\_shaped only), this contribution is compensated. In this case then, second order contributions dominate and the Multipoles O\_shape Error equation defined earlier can be applied. This is why it does not apply for the O\_shaped 1PP.

Again, it is the small size of the sensor that is the reason for this large difference between the two contributions. In any case, we realize that this sensor is also very sensitive to variations in mechanical tolerances, which makes measurements on PCB more complicated.

### 4.5 C-shaped simulation results

Here is the 3D model on which the simulations were performed.

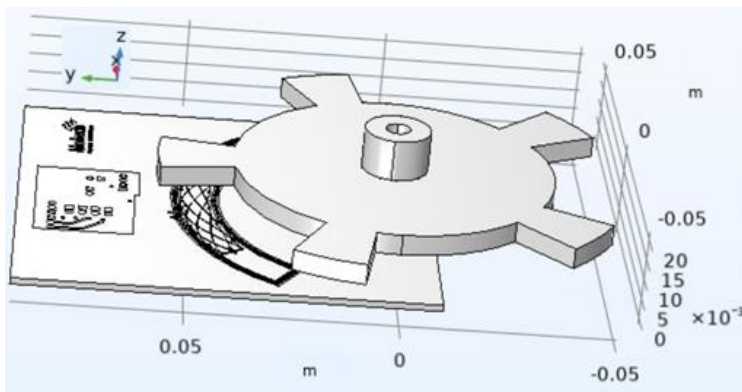


Figure 38. Simulation model C\_shaped 5PP

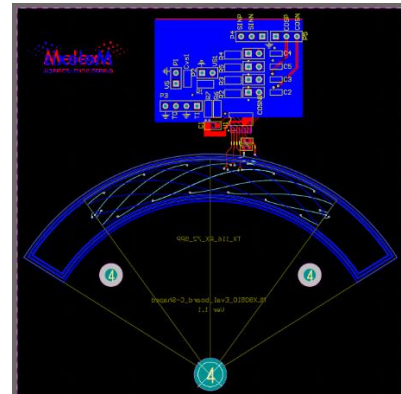


Figure 39. C\_shaped 5PP Altium layout

Above you can see the 3D model of the sensor and its target as presented in Comsol and its layout designed with Altium. It is the largest of the three simulated sensors, with an outer diameter of 114 mm. However, its nature of C\_shaped means that it only covers an arc of a circle measuring an angle of 72 ° (one electrical period).

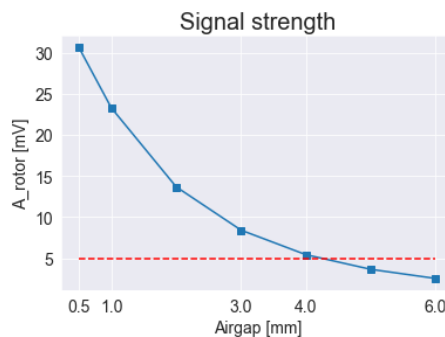


Figure 40. Signal strength vs Airgap C\_shaped 5PP

Here the sensor leaves its optimum operating zone above 4 mm of air gap. Although it is much larger than the O\_shaped 5PP, its reduced form only allows it to pick up a signal that is almost half as strong.

As for the two previous sensors, an on-axis accuracy measurement was made.

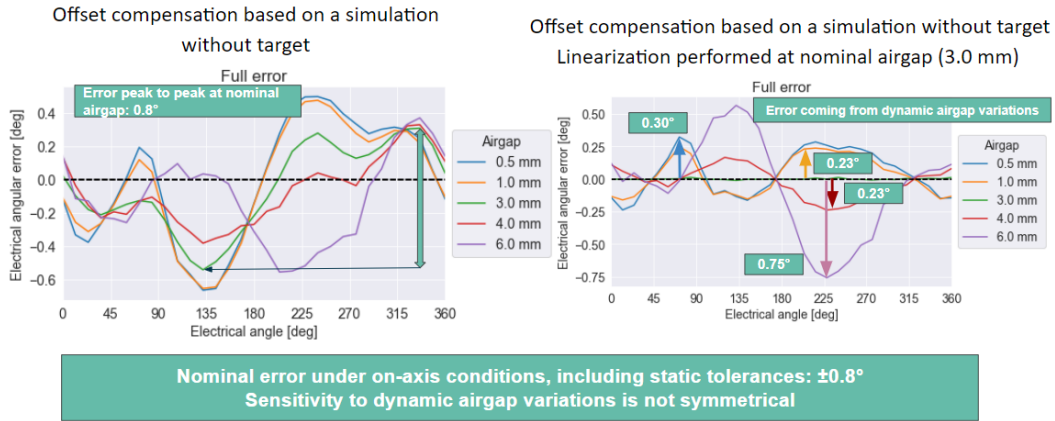


Figure 41. On-axis accuracy C-shaped 5PP

Under nominal conditions of use, the sensor has a precision comparable to that of the O-shaped 1PP, although it is more than 10 times larger. Moreover, the impact of the air gap variation on these measurements is significant and not symmetrical. The error is increasing a lot when we leave the zone of optimal use.

As for the previous sensor, here the contribution of the off axis and the tilt are independent because the sensor is no more symmetrical (no more compensation, so first order error is dominating). So, there are four configurations to simulate (longitudinal is x axis and transverse is y axis). The sensitivities are given in maximum values.

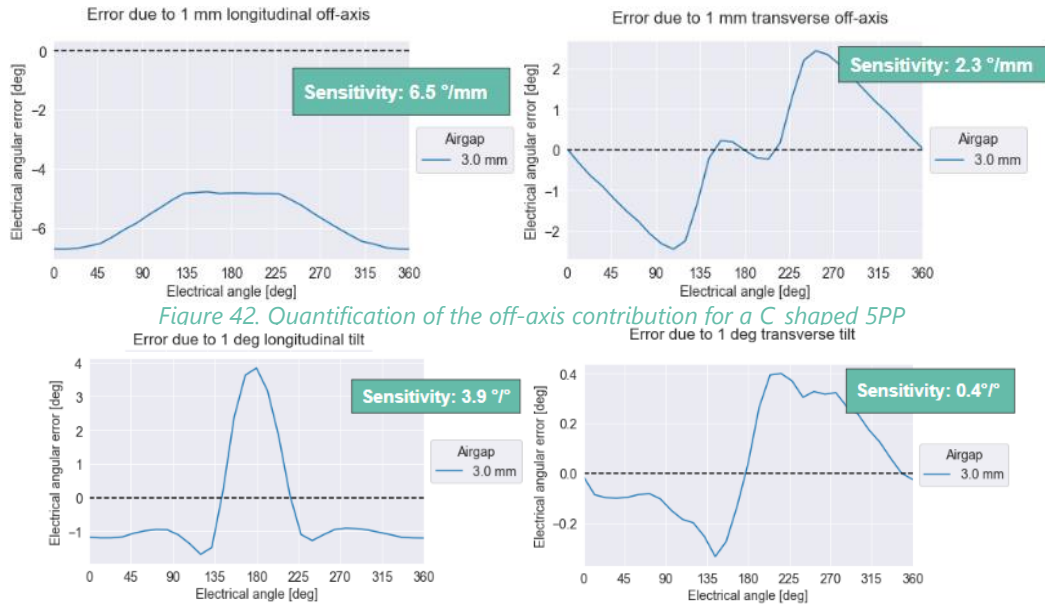


Figure 42. Quantification of the off-axis contribution for a C-shaped 5PP

Figure 43. Quantification of the tilt contribution for a C-shaped 5PP

All mechanical tolerances contributions to the measurement error are different because the sensor is not symmetrical. The y-axis contributions create zero average value errors because they only change the shape of the target surface that is detected by the sensor. On the other hand, on the x axis, large error offsets are created because deviations on this axis introduce measurement asymmetries.

## 4.6 Conclusion

With these simulations, we have shown that one of the sensors is much more accurate than the other two. Indeed, because of its shape, its size and its number of electrical periods, the 5PP O-shaped is the most accurate. The C-shaped sensor being chosen for its attractive price, there is a performance-price dilemma to solve. The O-shaped 1PP is used in very specific applications, which are not directly motor control and which require very small sensors. These results are therefore to be put in perspective with its intended use.

In this part we have studied the behavior of some sensors according to their shape. But to compare their versions MLX90510 and MLX90517, it is necessary to carry out some measurements.

# 5 Measures and MLX90510/MLX90517 evaluation

## 5.1 Measurement setup description

When Melexis engineers develop new sensors, which are ultimately intended to be sold, they have to test some of their characteristics to verify whether the values measured in real conditions are similar to the theoretical expected characteristics.

Some of these tests concern the sensitivity of the sensors to displacements relative to the measurement target (linear and angular displacements). From my side, I used the following setup and my work from my summer internship in Melexis last year to make measurements on the sensors previously simulated, and compare their behavior in mode MLX90510 and MLX90517.

In the Bevaix site Melexis lab, this is the setup to test the performances of inductive sensors.



Figure 44. Laboratory setup



Figure 45. Optical encoder

The HXP100-MECA, a High Precision 6-Axis Hexapod (a parallel kinematic motion device that provides six degrees of freedom: X, Y, Z, pitch, roll, and yaw) with its controller HXP100-ELEC-D.

Two different motors: the URS100BCC Rotation Stage that provides precision 360° continuous motion in a low profile package with its controller SMC100CC and the Maxon motor EC-i 40 449464 with its encoder EIL580P-SY06.5FF.01024.B to set a constant high rotation speed. The optical encoder is used to know the exact target position through time. this device gives the initial angle that can be compared to the one measured by the sensor. All the the results in this report are obtained with the first motor.



Figure 47. Low speed motor



Figure 46. National Instrument hardware

Two NI instruments to do some measurement on these tools (NI-9215: this device is an analog-to-digital converter which obtain data from the sensor with two coaxial cables, NI-9411 which measures and restitutes the data coming from the encoder, both are plugged in a cDAQ-9174, a programmable device which allows to synchronize their clocks.

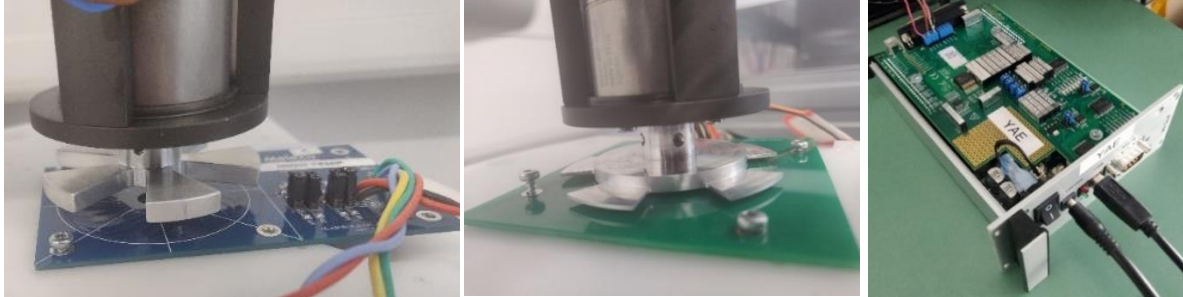


Figure 48. Two different O-shaped sensors with target and velocity motor

Figure 50. PTC04

The simulation of rotation to be measured is made by a motor and a metallic target just above the sensor. A last device is used to calibrate the sensors and more generally to read and modify certain part of their memory: The PTC04. It is used to program the EEPROM of the sensors.

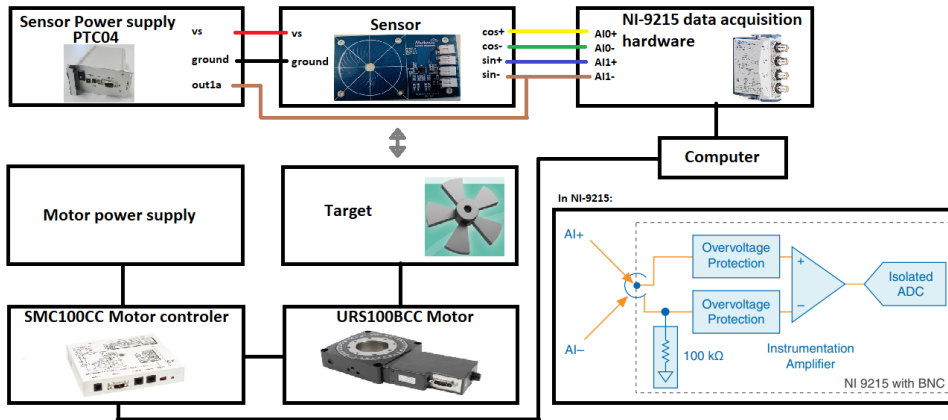


Figure 49. Block diagram of low speed setup

To align the setup there are 3 steps in order of accuracy: centering it to the accuracy of a human eye to reduce as much as possible the tilt and off axis in nominal position, measuring the signal strength at different positions as we will see in a next section, and finally using the following method:

The goal of the following steps is to determine the constant  $\zeta$  and all the mechanical tolerances introduced by the assembly procedure  $OA_x^0, OA_y^0, T_x^0, T_y^0, W_x^0, W_y^0, S_x^0, S_y^0$ . In a simulation all these tolerances are obviously zero. But it is different for real measurements. To obtain these values, it's necessary to apply the following misalignments to the setup, in addition of the initial ones, and measure the associate the error drifts.

- Additional x off-axis  $\Delta OA_x$ . Error induced:  $\Delta \epsilon_1 = \zeta \Delta OA_x [T_y^0 + S_y^0 \cos \alpha + S_x^0 \sin \alpha] = \Delta \epsilon^a_1 + \Delta \epsilon^b_1 \cos \alpha + \Delta \epsilon^c_1 \sin \alpha$
- Additional y off-axis  $\Delta OA_y$ . Error induced:  $\Delta \epsilon_2 = \zeta \Delta OA_y [-T_x^0 - S_x^0 \cos \alpha + S_y^0 \sin \alpha] = \Delta \epsilon^a_2 + \Delta \epsilon^b_2 \cos \alpha + \Delta \epsilon^c_2 \sin \alpha$
- Additional x tilt  $\Delta T_x$ . Error induced:  $\Delta \epsilon_3 = \zeta \Delta T_x [-OA_y^0 - W_y^0 \cos \alpha - W_x^0 \sin \alpha] = \Delta \epsilon^a_3 + \Delta \epsilon^b_3 \cos \alpha + \Delta \epsilon^c_3 \sin \alpha$
- Additional y tilt  $\Delta T_y$ . Error induced:  $\Delta \epsilon_4 = \zeta \Delta T_y [OA_x^0 + W_x^0 \cos \alpha - W_y^0 \sin \alpha] = \Delta \epsilon^a_4 + \Delta \epsilon^b_4 \cos \alpha + \Delta \epsilon^c_4 \sin \alpha$
- Additional x off-axis  $\Delta OA_x$  combined with an additional y tilt  $\Delta T_y$ . Error induced:  
 $\Delta \epsilon_5 = \zeta [\Delta OA_x \cdot T_y^0 + \Delta T_y \cdot OA_x^0 + \Delta OA_x \cdot \Delta T_y + (\Delta OA_x \cdot S_y^0 + \Delta T_y \cdot W_x^0) \cos \alpha + (\Delta OA_x \cdot S_x^0 + \Delta T_y \cdot W_y^0) \sin \alpha] = \Delta \epsilon^a_5 + \Delta \epsilon^b_5 \cos \alpha + \Delta \epsilon^c_5 \sin \alpha$

From the above errors, we can easily obtain all the unknown parameters:

- ❖  $\zeta = (\Delta\varepsilon^a_5 - \Delta\varepsilon^a_1 - \Delta\varepsilon^a_4)/(\Delta OA_x \cdot \Delta T_y)$
- ❖  $OA^0_x = \Delta\varepsilon^a_4/(\zeta \cdot \Delta T_y)$ ,  $OA^0_y = -\Delta\varepsilon^a_3/(\zeta \cdot \Delta T_x)$
- ❖  $T^0_x = -\Delta\varepsilon^a_2/(\zeta \cdot \Delta OA_y)$ ,  $T^0_y = \Delta\varepsilon^a_1/(\zeta \cdot \Delta OA_x)$
- ❖  $W^0_x = \Delta\varepsilon^b_4/(\zeta \cdot \Delta T_y) = -\Delta\varepsilon^c_3/(\zeta \cdot \Delta T_x)$ ,  $W^0_y = -\Delta\varepsilon^b_3/(\zeta \cdot \Delta T_x) = -\Delta\varepsilon^c_4/(\zeta \cdot \Delta T_y)$
- ❖  $S^0_x = -\Delta\varepsilon^b_2/(\zeta \cdot \Delta OA_y) = \Delta\varepsilon^c_1/(\zeta \cdot \Delta OA_x)$ ,  $S^0_y = \Delta\varepsilon^b_1/(\zeta \cdot \Delta OA_x) = \Delta\varepsilon^c_2/(\zeta \cdot \Delta OA_y)$

Once all the misalignments are known, they can be eventually corrected if the measurement setup allows for that (if it is precise enough for example). The  $\zeta$  value is now known and can be compared to the simulation value. A large part of this procedure come from a Melexis report wrote by Lugani, L [3].

All the scripts used to do some measurements on sensors are written in python.

Each PCB has two inputs (Vs and ground) and four outputs (sin+, sin-, cos+, cos-). Each pair of cable is connected with a coaxial cable, to the module NI-9215. Each sensor is an MLX90510, but it can be transformed into MLX90517 just by reprogramming the EEPROM of the chip with a PTC04

Then with the python library *nidaqmx*, it's possible to get an instantaneous measure of the voltage output, with a maximum frequency of 170 kHz. A measurement with two channels (two coaxial cables) take 6  $\mu$ s long. This conversion time is the time taken by ADC to convert the AI data to digital/quantized data. This conversion time is one of the reasons that makes measurements imprecise with the high-speed setup. This is why the majority of the analyzed data is obtained with the low-speed setup. This is a differential measure. The Sinus value is obtain doing sin+ + sin- and same for cosine. With these values, it's easy to obtain an angle with arctan function, and then compare this angle with the reference one, given by the precise motor. It's a step by step measurement, with steps of 1 °.

## 5.2 Description of post processing algorithms

For a given sensor, the procedure is automated with a Python script. You have to give an initial position to the sensor; the desired mechanical tolerances and the setup starts moving. It takes an initial measurement which serves as a reference, then varies the Air Gap, the tilt on two axes, the off axis on two axes, then a combination of tilt and off axis. This process is repeated 3 times to remove noise and measurement errors as much as possible. This whole procedure is repeated 4 times: Once in uncalibrated MLX90517 mode, then with the sensor calibrated using the PTC04 (the calibration parameters have been determined before), then the sensor is switched to uncalibrated MLX90510 mode (modification in the IC) and finally in calibrated version again. All measured data is compiled into csv files.

Once the raw data is obtained, it is possible to use du post processing algorithms in the ECU to try to obtain a better-quality signal. These algorithms are effective for the MLX90517 output. One of the best methods to do this is called: The Min-Max method (I took an example in an Infineon report [2].)

The first step is to create an average electrical period on Sine and Cosine for all electrical period of the whole set of measurement. We name them Y (for Sine) and X (for Cosine) as X. The figure opposite shows an exaggerated representation of the Sinus vs Cosine curve before correction. There are some problems of offsets, amplitude and orthogonality. To correct them we introduce some quantities.

Offsets:  $O_x = \frac{X_{max} + X_{min}}{2}$ ,  $O_y = \frac{Y_{max} + Y_{min}}{2}$ , and amplitudes:  $A_x = \frac{X_{max} - X_{min}}{2}$ ,  $A_y = \frac{Y_{max} - Y_{min}}{2}$ , then we apply the offset correction:  $X_1 = X - O_x$ ,  $Y_1 = Y - O_y$ , then we normalize the amplitude:  $X_2 = \frac{X_1}{A_x}$ ,  $Y_2 = \frac{Y_1}{A_y}$ .

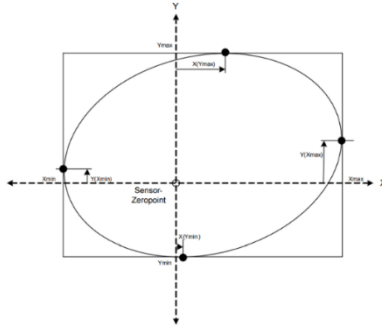


Figure 51. Sine (Y) vs Cosine (X)

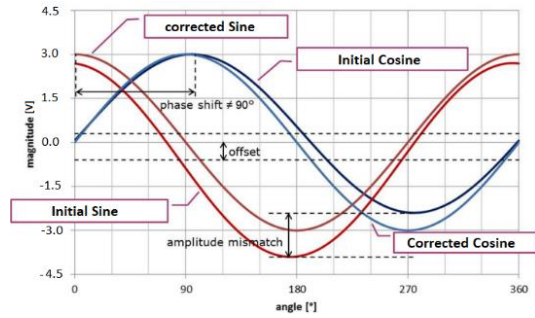


Figure 52. Initial and corrected signal

Then there are different more or less complicated methods to correct orthogonality errors that we have not explained here to save time. In any case, we will realize later that for our measurements they are very low and correcting them does not improve the signal.

Here is what these calculations are supposed to modify:

To analyze the data with this method and obtain certain result curves, another python code is used to read the csv files and compare the results according to the desired parameters. These results will be presented later in this report.

### 5.3 O-shaped (5PP) MLX90517 and MLX90510

#### 5.3.1 Measurement procedure, results and comparison with simulation

The sensors used are those whose photographs and layout were shown in the previous sections. It has an external diameter of 54 mm, the measurements were made with a nominal air gap of 5 mm. The gain of the AGC is left free between 0 and 4. The sensor is first placed in uncalibrated MLX90517 mode.

To obtain the most relevant measurements possible, the first step is to center the sensor and the motor using the hexapod. The first part is done with the naked eye, you have to try to get as close as possible to a situation where the sensor and the target are parallel (remove any tilt) and with their axis of rotation aligned (remove any off-axis), this is to avoid certain errors that we will discuss later.

These sensors can be aligned by hand, it works well but it is not enough to make proper measurements. One of the most accurate and efficient methods that can be used is signal strength measurement. Another alignment method is explained in the part on simulations, but requires complete results of measurements on which we will look.

Take the example of a variation of off axis on the X axis. The sensor is perfectly symmetrical so if the initial off axis is zero, an equal displacement in absolute value in one direction or another must induce the same variation of the value of Arotor.

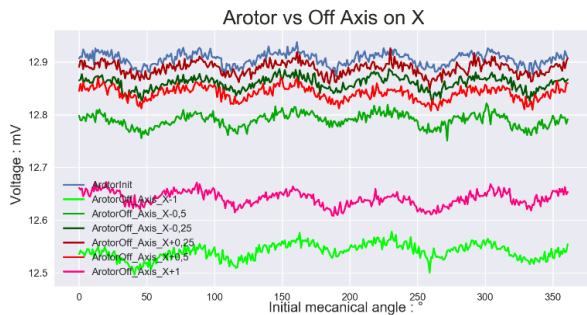


Figure 53. O\_shaped 5PP Arotor curves with X-Off\_Axis variation before centering

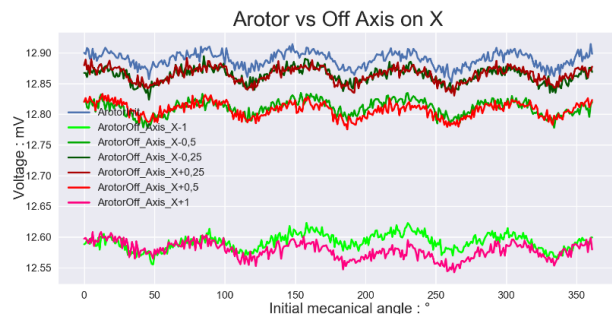


Figure 54. O\_shaped 5PP Arotor curves with X-Off\_Axis variation after centering

With a first measurement we realize that this is not the case, and then by moving slightly on the side with the associated values closest to the initial curve (here the positive X direction), we correct this asymmetry.

By repeating the process for the Y axis in off axis and the two axes in tilt, we obtain a much more precisely centered setup. This can be seen by comparing the measurements of Arotor at the zero position for the two situations.

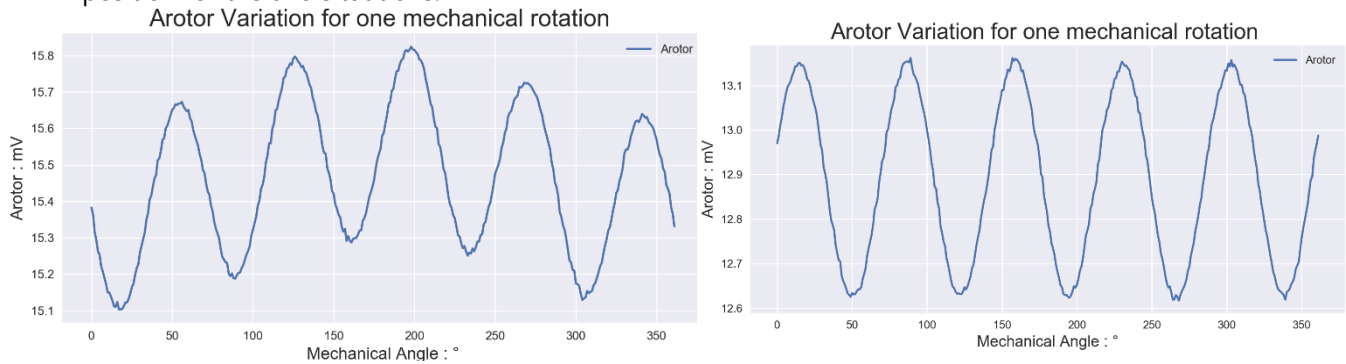


Figure 55. O-shaped 5PP Arotor at nominal Air\_gap before centering Figure 56. O-shaped 5PP Arotor at nominal Air\_gap after centering

On these Arotor curves, there is a 0.2 mV modulation on a mechanical period (360°), linked to the mechanical tolerances, which we try to eliminate by centering the setup. This modulation comes from the slight wobble and skew present on the setup, whose contribution to the overall error is amplified by tilt and off axis (multiplication in the error formula). However, there is still a 0.5 mV modulation on an electrical period (72°). This is because the offset compensation has not yet been done, so there is no need to remove this error at this stage.

These signal strength measurements are made using a PTC04 which measures the three-phase differential signals explained in simulations (digitized signals) and applies the mathematical formulas of the 4.2 section to it.

Before moving on to the error measurements, it is necessary to check that our nominal placement respects the good operating conditions of the sensor. Indeed, to be in these conditions, this sensor must measure a signal strength greater than 5 mV. In our case, this corresponds to air gap values of less than 7 mm. These are exactly the values that were found in simulation (Figure 29).

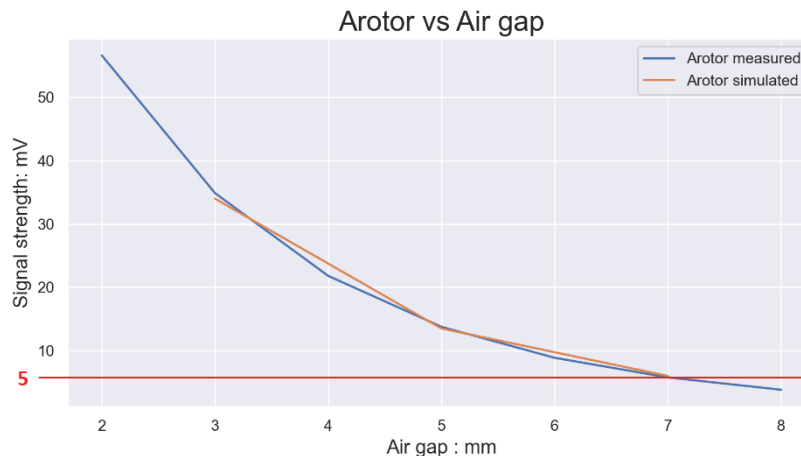


Figure 57. O-shaped 5PP Measured signal strength vs Air Gap

Thanks to the data measured by the PTC04 we can also obtain the phase, which by comparing it with the initial angle (by putting the two curves in a comparable form) gives a measurement error at the output of the coils, which it is possible to compare to the error at the output of the sensor.

The error that comes from the three-phase signals of the coils (phase) are not affected by disturbances that the chip can produce, the errors just come from the coils or the front end. The error at the output of the sensor (differential) is affected by these disturbances. We can therefore compare them.

As we can see in Figure 59, these errors are globally identical if we exclude a certain noise, which confirms that it comes entirely from the measurement and not from the IC, back end does not add any error.

At the same time, it is possible to compare these errors with that obtained in a single-ended configuration (the wires measuring sin- and cos- are connected to ground). A configuration used by some customers because it is easier to set up. This method requires us to do some post processing because the sin and cos signals are entirely positive. Either we remove from sin and cos simply their common average value as a naive method. (green curve), or we can apply the Min\_Max method to sin and cos (red curve), which obviously gives better results but much less efficient than a differential measurement of an MLX90517 with the Min\_Max method applied as we will see in the following.

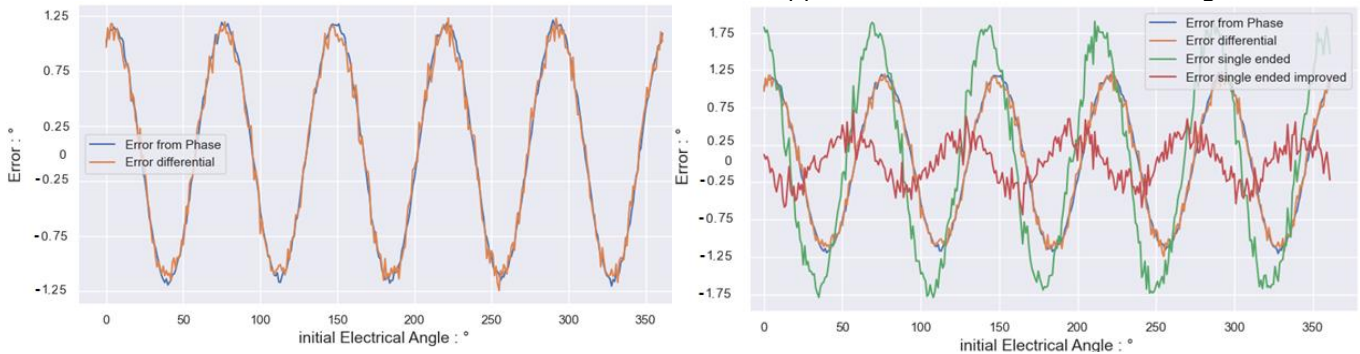


Figure 59. Error at coil (from Phase) and IC output (differential) Figure 58. Differential error compared with single ended measures

One of the main differences between the MLX90510 and the MLX90517 is the amplitude of the output signals. In MLX90510 mode, no matter how strong the signal is, the sensor will return sine and cosine signals ranging from -3V to 3V, while in MLX90517 mode, the amplitude of the signals depends on the signal strength (so air gap) and AGC gain:

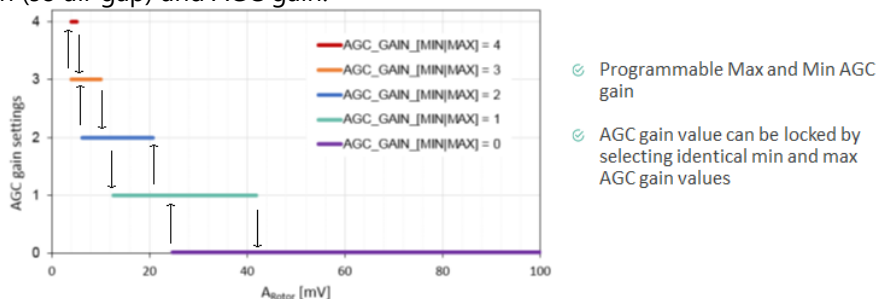


Figure 60. MLX90517 Automated Gain Control (AGC) principle

Indeed, with this staircase function, the lower the Arotor, the more the signal is amplified with this AGC\_GAIN. This effect can be easily observed by looking at the output signal of the sensor in mode MLX90517 by varying the air gap.

Without gain, the Sinus curves should have a large amplitude with a small air gap (like SinAir\_gap-3) and the reverse for a large air gap but this is not the case. We can also observe a "jump" in gain on the SinAir\_gap+3 curve, surely linked to a residual tilt. This type of jump also takes place on the Cosine curve, which therefore has no impact on the value of the angle but makes it difficult to use a linearization method such as Min\_Max.

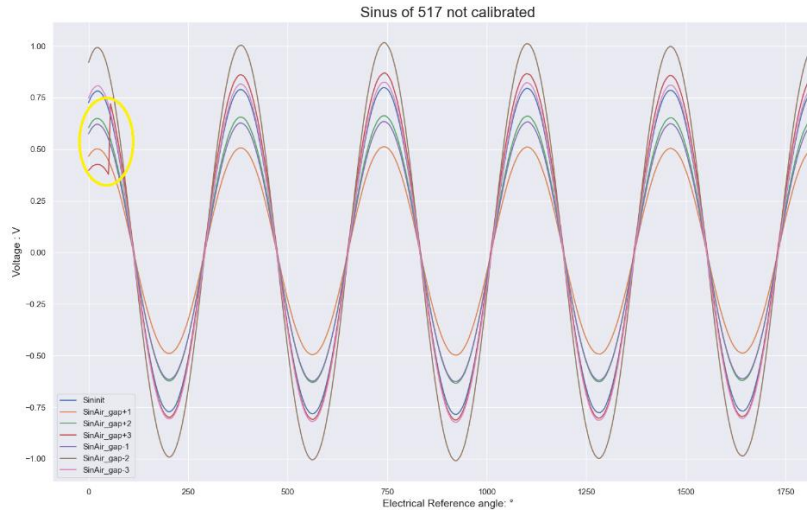


Figure 61. O-shaped 5PP Output Sinus for different Air Gap

To counter this effect when using an MLX90517, it is possible to restrict the AGC gain value. However, this choice can be problematic if, in practice, the installation on which the sensor is fixed is subject to a lot of vibrations (like in a car) which can occasionally increase the air gap and drastically reduce the amplitude of the signal. output, and therefore its quality.

The following curves represent the measurement error at a nominal air gap of 5 mm, trying to have as little tilt and off axis as possible, all over an average electrical period. In black dotted line we have the initial error, in blue the error associated with the data to which the Min\_Max method was applied, in orange the version with Min\_Max and an amplitude normalization, and in green dotted line, a last version with Min\_Max , amplitude normalization and orthogonality correction.

Curve (a) corresponds to the sensor initialized in mode MLX90517 and not calibrated. The initial error is quite large, but the Min\_Max method makes it possible to greatly reduce it (the initial error is divided by 10). However, normalizing the amplitude and correcting the orthogonality error does not improve the result. Curve (b) corresponds to the sensor initialized in mode MLX90510 and not calibrated the initial error is identical to curve A which shows a certain equivalence between these two operating modes in this case. For this configuration, on the other hand, the Min\_Max Method is completely useless. This result was expected because the MLX90510 mode already corrects offsets, amplitude and orthogonality in the chip. In this case then the MLX90517 mode is more interesting.

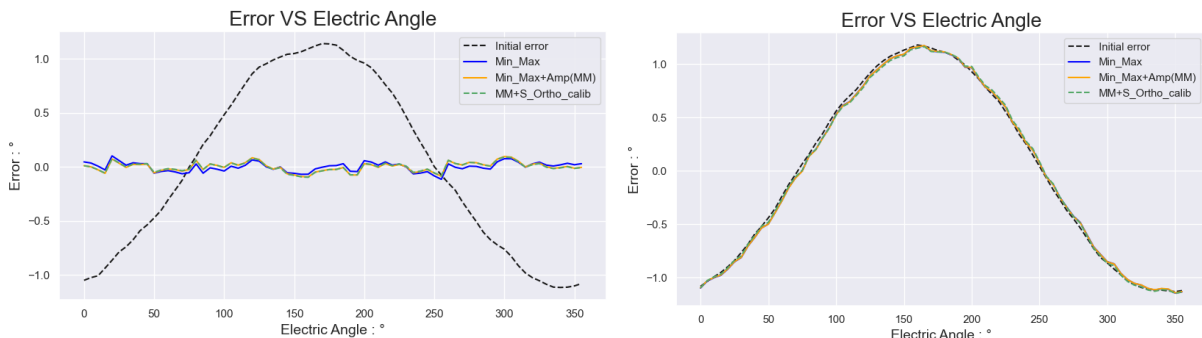


Figure 62. 72-degree average Error at nominal position for an O-shaped 5PP MLX90517(a) and MLX90510(b)

However, this mode of operation is not recommended for real use. With a PTC04, it is possible to calibrate the sensor, and therefore to program the chip, to reduce a large part of the primary sources of error. After calibration (curve c and d), the initial errors in modes MLX90517 and MLX90510 are greatly reduced. In this case, we can note a good advantage of mode MLX90510 (30%), which is surely linked to the measurement noise of mode MLX90517, which we will discuss a little later.

On the other hand, the Min\_Max method, after calibration, has very little interest. Here it slightly improves the results, but in case of slight residual mechanical tolerance, it can have the opposite effect. However, we note that in this case, calibrating the sensor in MLX90517 mode makes it nearly 9% less efficient than using it uncalibrated with a Min\_Max correction. This observation can once again be reversed with slightly different residual mechanical tolerances because the error values are very low. What should be remembered is that the calibration and the Min\_Max algorithm have rather similar performances for this MLX90517.

If we are interested in the performance of the two versions of this O\_shape, we notice that the basic peak-to-peak error of the MLX90517 is around 0.3°, and 0.2° with the application of Min\_Max which is ultimately equivalent to the performance of the MLX90510 (0.2°). The value found during the On-axis accuracy simulation (Figure 30) was 0.09°. The measured error is therefore approximately twice that of the simulated one. This discrepancy is explained on the one hand by the unintended residual mechanical tolerances, and on the other by the measurement noise which has a non-negligible impact for such small error values. In reality, these measurements are quite consistent with the simulations.

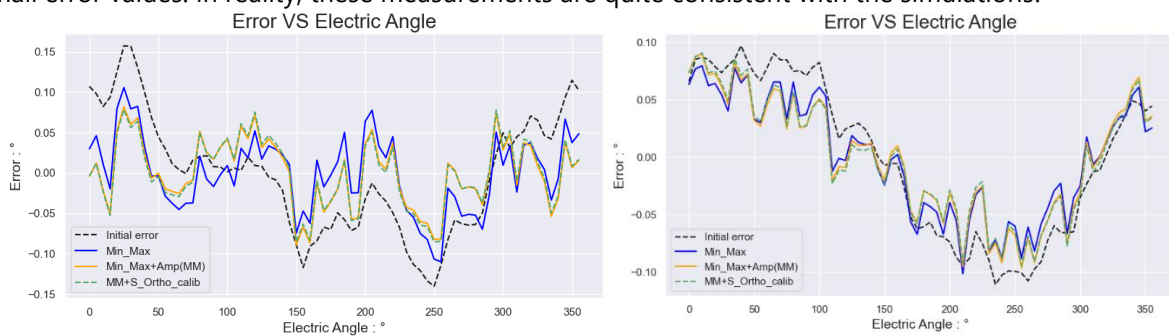


Figure 63. 72-degree average Error at nominal position for an O\_shaped 5PP MLX90517(c) and MLX90510(d) calibrated without rotor

However, this calibration must be carried out individually for each sensor, with a PTC04. This can be a problem for industrial productions. This is one of the reasons why some customers don't want to bother with this step. In this case the MLX90517 makes sense.

Then we can focus on the behavior of the two sensors relative to the variations of the mechanical tolerances. In the following curves, a mechanical period is explained (therefore in this case, 5 electrical periods). This makes it possible to realize the periodic or non-periodic behavior of the sensor.

Let's start with the air gap.

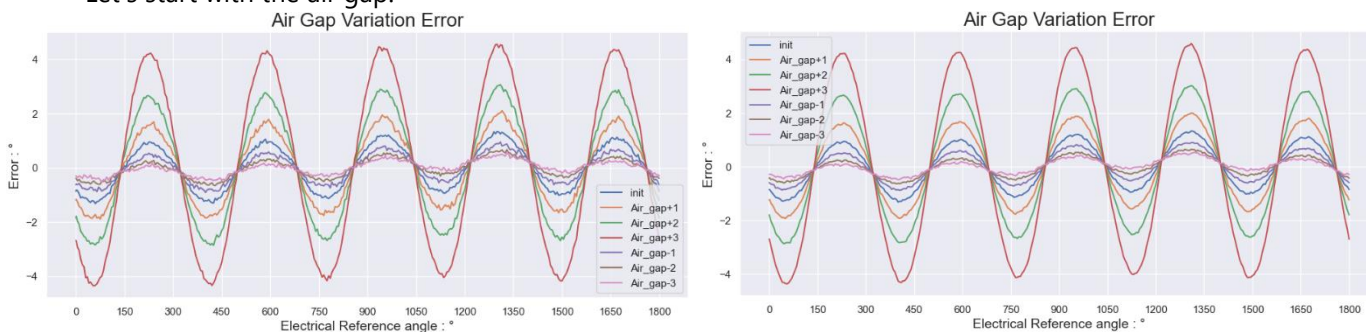


Figure 64. 360-degree error in function of Air Gap variation for an O\_shaped 5PP MLX90517(a) and MLX90510(b) uncalibrated

Note that the bulk of the error is perfectly periodic, the curve is similar to a sinusoidal function whose amplitude is directly related to the air gap. The further the target is from the sensor, the greater the amplitude of the error and vice versa. A linear and expected evolution which is substantially the same whether we place the sensor in MLX90517 or in MLX90510 mode. There is an effect which we can already observe here and which will follow us on all the results is the presence of a noticeably higher noise in MLX90517 mode.

This effect is mainly linked to the low amplitude of the output signal (<2V) compared to MLX90510 (=6V). The perfectly periodic nature of the signal allows us to characterize the noise at the output of the sensor in its different modes. By plotting this graph in its non-periodic version, we obtain:

A noise with an average amplitude of about 0.2° for the MLX90517 and 0.08° for the MLX90510 (2.5 times less), which obviously limits the maximum precision of the sensor.

Now let's look at the behavior of the calibrated sensor in the face of air gap variations, here the noise is of much greater importance, and it is very difficult to compare the results obtained with the simulations.

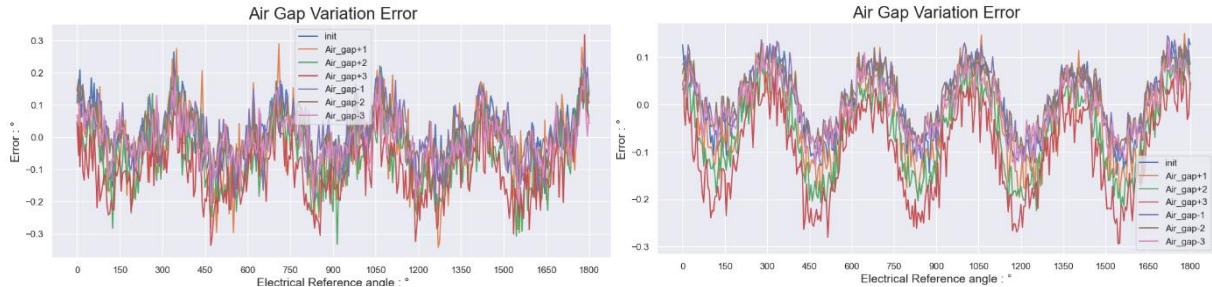


Figure 66. 360-degree error in function of Air Gap variation for an O-shaped 5PP MLX90517(c) and MLX90510(d) calibrated

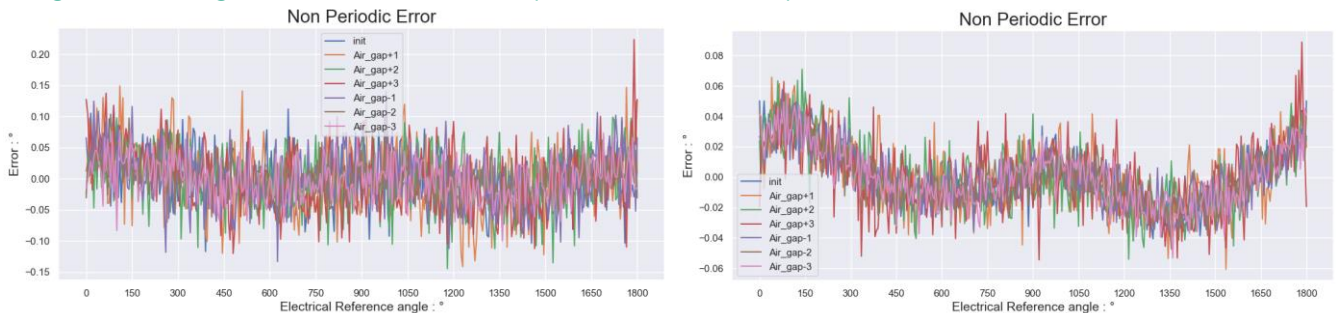


Figure 65. 360-degree non-periodic error in function of Air Gap variation for an O-shaped 5PP MLX90517(a) and MLX90510(b) uncalibrated

Once calibrated, the sensor drastically reduces the variation for the amplitude of the error peaks. For all the air gap values, we are very close to the calibrated nominal air gap curve, and it is difficult to differentiate them because of the ambient measurement noise. Note that some non-periodic error remains as we can see in the Figure 67, representing a measurement on this sensor with slightly higher residual mechanical tolerances (linked to Figure 55a).



Figure 67. Version with unwanted tolerances

To compare the influence of the air gap on the measurements of this sensor after calibration with the values found in simulation, it is preferable to select the periodic error curve of the MLX90510 to remove as much noise as possible. We then remove the nominal error value from all the curves as in simulation so that it is more readable. We then realize that there is a maximum difference of 0.11° in the measurements at air gaps of 5 mm (blue) and 7 mm (green) against 0.17° in simulation and 0.17° difference between the curves at 7mm (green) and 3mm (purple) of air gap against 0.23° in simulation. It is surprising to note but our simulations were pessimistic. The real rotorless calibration performed a little better than the simulation. Small deviations that can be explained by the differences in conditions between simulation and measurement (slight mechanical tolerances on the measurement setup).

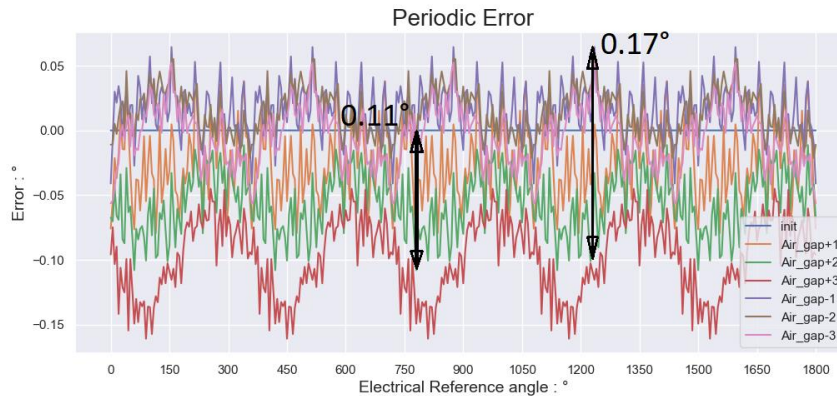


Figure 68. 360-degree periodic error in function of Air Gap variation for an O-shaped 5PP MLX90510 calibrated. The Min\_Max method gives results similar to the calibration with even fewer differences between the curves corresponding to the different air gaps. However, for the Air\_gap+3 curve, corresponding to the maximum air gap of this measurement set, the Min\_Max method gives poor results because of the AGC gain jump at the edge of the measurement range, which modifies the extrema of the sine and cosine outputs. One way to solve this problem is to constrain the gain to a certain value if you know in advance the strength of the signal in real use.

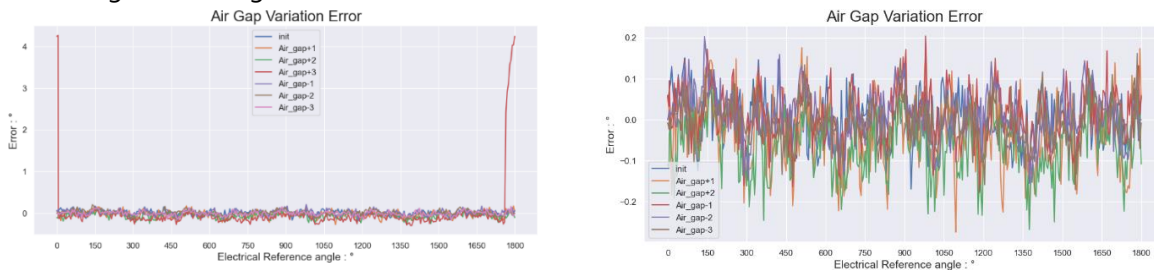


Figure 69. 360-degree Min\_Max error in function of Air Gap variation for an O-shaped 5PP MLX90517 uncalibrated with nominal Air Gap + 3 curve (a) and without it (b)

To analyze the curves representing the error as a function of the variations in tilt and off axis, it is preferable to use a form of graph in which the initial error is subtracted from all the other curves. This makes reading the error variations clearer. For example, in the following figures, we can observe that a tilt on U (an y-tilt in the referential of the hexapod) causes a periodic offset (in degrees) of the curves between them. But difficult to compare this offset in the uncalibrated MLX90517 version and these same data with Min\_Max applied.

After subtracting the initial error values, it is easy to see that the uncalibrated version, the one with Min\_Max applied, or the calibrated version all show the same behavior. These algorithms have no impact on the differences between the curves for tilts or off axis.

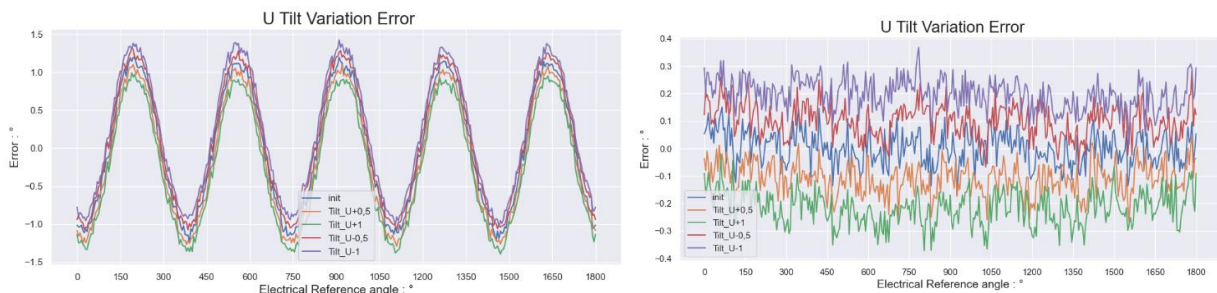


Figure 70. 360-degree error without (a) and with (b) subtraction of nominal value in function of y-tilt variation for an O-shaped 5PP MLX90517 uncalibrated

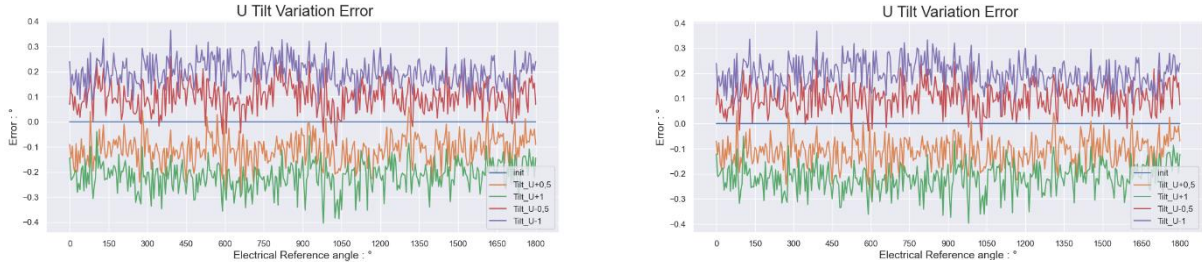


Figure 71. 360-degree error in function of y-tilt variation for an O\_shaped 5PP MLX90517 uncalibrated(a) and Min\_Max

The behavior of the MLX90510 is identical, regardless of its version and differs only in the presence of less noise.

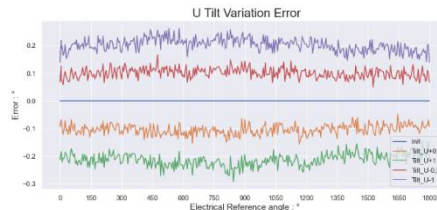


Figure 72. 360-degree MLX90510 error

We then wonder what causes these discrepancies. Especially when remembering Multipoles O\_shape Error equation according to the mechanical tolerances, we understand that a tilt or an off axis alone cannot create a measurement error.

In reality there are always slight residual tilts off axis, wobble and skew at the initial position and this measurement reveals them. Each deliberately applied tilt combines with a residual off axis to create an error and vice versa. But then how to quantify these residual mechanical tolerances?

The protocol described in the simulation part must be reused. We first need the error curves associated with the tilt variation and with a fixed off axis.

In an ideal case, the two curves with an x-tilt (tilt on V) and an x-off axis should have a zero mean and the other two curves with a y-tilt (tilt on U) and an x-off axis should have the same mean in absolute value. This is obviously not the case and this will allow us to calculate all our initial parameters ( $OA_x^0$ ,  $OA_y^0$ ,  $T_x^0$ ,  $T_y^0$ ,  $W_x^0$ ,  $W_y^0$ ,  $S_x^0$ ,  $S_y^0$  and  $\zeta$ ).

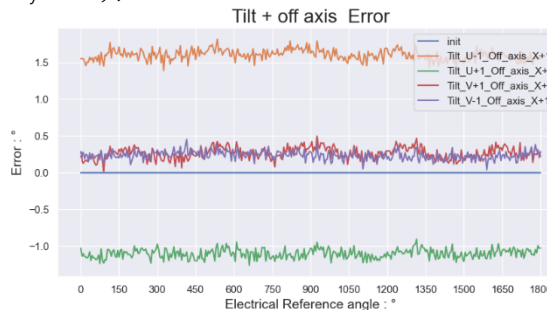


Figure 73. 360-degree error in function of tilt variation with positive x-off-axis for an O\_shaped 5PP MLX90517 uncalibrated

The results are quite similar for the MLX90510, for the following calculations we will start with the data from this one because the noise is lower (graphs are clearer).

For each curve, a python tool (scipy.optimize.curve\_fit) is used to approximate the error by a function with the form:  $a + b \cos \alpha + c \sin \alpha$

For the MLX90510, we need:

- Additional x off-axis  $\Delta OA_x = +1\text{mm}$  Error induced:  $\Delta \epsilon_1 = \zeta \Delta OA_x [T_y^0 + S_y^0 \cos \alpha + S_x^0 \sin \alpha] = \Delta \epsilon^a_1 + \Delta \epsilon^b_1 \cos \alpha + \Delta \epsilon^c_1 \sin \alpha = \mathbf{0.261} - 0.0329 \cos \alpha - 0.00780 \sin \alpha$  °

- Additional y off-axis  $\Delta OA_y = +1\text{mm}$ . Error induced:  $\Delta \epsilon_2 = \zeta \Delta OA_y [-T_x^0 - S_x^0 \cos \alpha + S_y^0 \sin \alpha] = \Delta \epsilon^a_2 + \Delta \epsilon^b_2 \cos \alpha + \Delta \epsilon^c_2 \sin \alpha = \mathbf{0.505} - 0.0333 \cos \alpha - 0.00223 \sin \alpha$  °

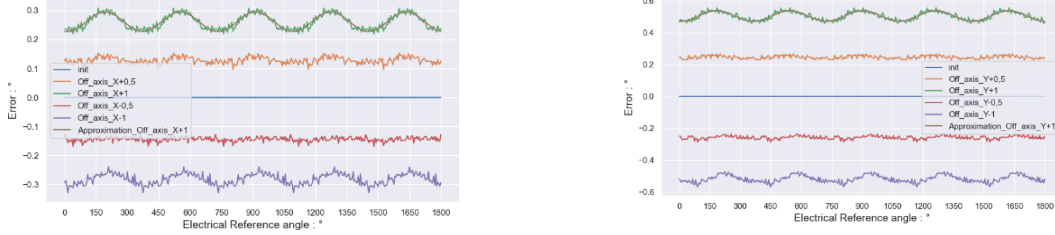


Figure 74. 360-degree periodic error in function of x-off-axis (a) and y-off-axis (b) variation for an O-shaped 5PP MLX90510 uncalibrated with approximation

- Additional x tilt  $\Delta T_x = +1^\circ$ . Error induced:  $\Delta \epsilon_3 = \zeta \Delta T_x [-OA_y^0 - W_y^0 \cos \alpha - W_x^0 \sin \alpha] = \Delta \epsilon^a_3 + \Delta \epsilon^b_3 \cos \alpha + \Delta \epsilon^c_3 \sin \alpha = 0.0155 - 0.0123 \cos \alpha - 0.000332 \sin \alpha$  °

- Additional y tilt  $\Delta T_y = 1^\circ$  or  $-1^\circ$ . Error induced:  $\Delta \epsilon_4 = \zeta \Delta T_y [OA_x^0 + W_x^0 \cos \alpha - W_y^0 \sin \alpha] = \Delta \epsilon^a_4 + \Delta \epsilon^b_4 \cos \alpha + \Delta \epsilon^c_4 \sin \alpha = \mathbf{-0.214} + 0.00791 \cos \alpha - 0.00819 \sin \alpha$  ° for  $\Delta T_y = 1^\circ$  or  $\mathbf{0.203} - 0.00570 \cos \alpha + 0.00792 \sin \alpha$  ° for  $\Delta T_y = -1^\circ$

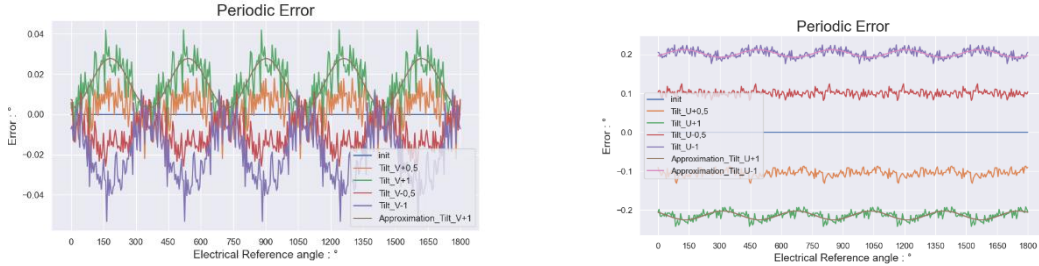


Figure 75. 360-degree periodic error in function of x-tilt (a) and y-tilt (b) variation for an O-shaped 5PP MLX90510 uncalibrated with approximation

- Additional x off-axis  $\Delta OA_x = 1\text{mm}$  combined with an additional y tilt  $\Delta T_y = 1^\circ$  or  $-1^\circ$ . Error induced:  $\Delta \epsilon_5 = \zeta [\Delta OA_x T_y^0 + \Delta T_y OA_x^0 + \Delta OA_x \Delta T_y + (\Delta OA_x S_y^0 + \Delta T_y W_x^0) \cos \alpha + (\Delta OA_x S_x^0 + \Delta T_y W_y^0) \sin \alpha] = \Delta \epsilon^a_5 + \Delta \epsilon^b_5 \cos \alpha + \Delta \epsilon^c_5 \sin \alpha = \mathbf{-1.12} - 0.0170 \cos \alpha + 0.0155 - 0.0398 \sin \alpha$  ° for  $\Delta T_y = 1^\circ$  or  $\mathbf{1.58} - 0.0501 \cos \alpha + 0.0155 + 0.0192 \sin \alpha$  ° for  $\Delta T_y = -1^\circ$

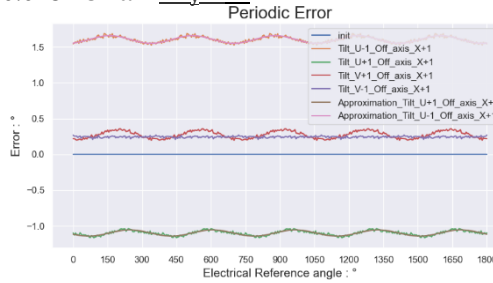


Figure 76. 360-degree periodic error in function of tilt variation with positive x-off-axis for an O-shaped MLX90510 uncalibrated with approximation

From the above errors, we can then easily obtain all the unknown parameters:

- ❖  $\zeta = (\Delta \epsilon^a_5 - \Delta \epsilon^a_1 - \Delta \epsilon^a_4) / (\Delta OA_x \Delta T_y) = -1.167^\circ$  if we take  $\Delta OA_x = 1\text{mm}$  and  $\Delta T_y = 1^\circ$  (1.48% deviation from the simulation value).
- ❖  $\zeta = (\Delta \epsilon^a_5 - \Delta \epsilon^a_1 - \Delta \epsilon^a_4) / (\Delta OA_x \Delta T_y) = -1.121^\circ$  if we take  $\Delta OA_x = 1\text{mm}$  and  $\Delta T_y = -1^\circ$  (2.57% deviation from the simulation value)

In the simulation we found that  $\zeta = 1.15^\circ$ . The measurements are therefore almost symmetrical and are slightly different from the simulation results.

Same procedure for the MLX90517:

- Additional x off-axis  $\Delta OA_x = +1\text{mm}$  Error induced:  $\Delta \varepsilon_1 = \zeta \Delta OA_x [T_y^0 + S_y^0 \cos \alpha + S_x^0 \sin \alpha] = \Delta \varepsilon^{a_1} + \Delta \varepsilon^{b_1} \cos \alpha + \Delta \varepsilon^{c_1} \sin \alpha = \mathbf{0.254} - 0.0327 \cos \alpha - 0.00438 \sin \alpha$  °

- Additional y off-axis  $\Delta OA_y = +1\text{mm}$ . Error induced:  $\Delta \varepsilon_2 = \zeta \Delta OA_y [-T_x^0 - S_x^0 \cos \alpha + S_y^0 \sin \alpha] = \Delta \varepsilon^{a_2} + \Delta \varepsilon^{b_2} \cos \alpha + \Delta \varepsilon^{c_2} \sin \alpha = \mathbf{0.499} - 0.0385 \cos \alpha - 0.00134 \sin \alpha$  °

- Additional x tilt  $\Delta T_x = +1^\circ$ . Error induced:  $\Delta \varepsilon_3 = \zeta \Delta T_x [-OA_y^0 - W_y^0 \cos \alpha - W_x^0 \sin \alpha] = \Delta \varepsilon^{a_3} + \Delta \varepsilon^{b_3} \cos \alpha + \Delta \varepsilon^{c_3} \sin \alpha = \mathbf{0.0111} - 0.0122 \cos \alpha + 0.000383 \sin \alpha$  °

- Additional y tilt  $\Delta T_y = 1^\circ$  or  $-1^\circ$ . Error induced:  $\Delta \varepsilon_4 = \zeta \Delta T_y [OA_x^0 + W_x^0 \cos \alpha - W_y^0 \sin \alpha] = \Delta \varepsilon^{a_4} + \Delta \varepsilon^{b_4} \cos \alpha + \Delta \varepsilon^{c_4} \sin \alpha = \mathbf{-0.217} + 0.0107 \cos \alpha - 0.00282 \sin \alpha$  ° for  $\Delta T_y = 1^\circ$  or  $\mathbf{0.199} - 0.00586 \cos \alpha + 0.00733 \sin \alpha$  ° for  $\Delta T_y = -1^\circ$

- Additional x off-axis  $\Delta OA_x = 1\text{mm}$  combined with an additional y tilt  $\Delta T_y = 1^\circ$  or  $-1^\circ$ . Error induced:  $\Delta \varepsilon_5 = \zeta [\Delta OA_x T_y^0 + \Delta T_y OA_x^0 + \Delta OA_x \Delta T_y + (\Delta OA_x S_y^0 + \Delta T_y W_x^0) \cos \alpha + (\Delta OA_x S_x^0 + \Delta T_y W_y^0) \sin \alpha] = \Delta \varepsilon^{a_5} + \Delta \varepsilon^{b_5} \cos \alpha + \Delta \varepsilon^{c_5} \sin \alpha = \mathbf{-1.11} - 0.0170 \cos \alpha + 0.0111 - 0.0398 \sin \alpha$  ° for  $\Delta T_y = 1^\circ$  or  $\mathbf{1.59} - 0.0501 \cos \alpha + 0.0111 + 0.0192 \sin \alpha$  ° for  $\Delta T_y = -1^\circ$

From the above errors, we can then easily obtain all the unknown parameters:

- ❖  $\zeta = (\Delta \varepsilon^{a_5} - \Delta \varepsilon^{a_1} - \Delta \varepsilon^{a_4}) / (\Delta OA_x \Delta T_y) = -1.148$  ° if we take  $\Delta OA_x = 1\text{mm}$  and  $\Delta T_y = 1^\circ$  (0.165% deviation from the simulation value)
- ❖  $\zeta = (\Delta \varepsilon^{a_5} - \Delta \varepsilon^{a_1} - \Delta \varepsilon^{a_4}) / (\Delta OA_x \Delta T_y) = -1.139$  ° if we take  $\Delta OA_x = 1\text{mm}$  and  $\Delta T_y = -1^\circ$  (0.922% deviation from the simulation value)

In the simulation we found that  $\zeta = 1.15^\circ$ . The measurements are therefore almost perfectly symmetrical and fully agree with the simulations.

We note that the MLX90517 has a behavior much closer to that of the simulations than the MLX90510. All the modifications made to the output signal of the coils by the IC of the MLX90510 modify the influence of the mechanical tolerances on the precision of the sensor. However, these differences are minimal and we can say that the performance of the two sensors is very similar if we forget the higher noise in the MLX90517.

Now, with the collected data, we can estimate the residual mechanical tolerances that were applied to the initial position on the measurement setup.

For this, we take:  $\Delta OA_x = 1\text{mm}$  and  $\Delta T_y = 1^\circ$ .

- ❖  $OA_x^0 = \Delta \varepsilon^{a_4} / (\zeta \Delta T_y) = -0.189$  mm,  $OA_y^0 = -\Delta \varepsilon^{a_3} / (\zeta \Delta T_x) = -0.00962$  mm
- ❖  $T_x^0 = -\Delta \varepsilon^{a_2} / (\zeta \Delta OA_y) = -0.434$  °,  $T_y^0 = \Delta \varepsilon^{a_1} / (\zeta \Delta OA_x) = 0.221$  °
- ❖  $W_x^0 = \Delta \varepsilon^{b_4} / (\zeta \Delta T_y) = -\Delta \varepsilon^{c_3} / (\zeta \Delta T_x) \approx 0.003$  mm
- ❖  $W_y^0 = -\Delta \varepsilon^{b_3} / (\zeta \Delta T_x) = -\Delta \varepsilon^{c_4} / (\zeta \Delta T_y) \approx 0.007$  mm
- ❖  $S_x^0 = -\Delta \varepsilon^{b_2} / (\zeta \Delta OA_y) = \Delta \varepsilon^{c_1} / (\zeta \Delta OA_x) \approx 0.01^\circ$
- ❖  $S_y^0 = \Delta \varepsilon^{b_1} / (\zeta \Delta OA_x) = \Delta \varepsilon^{c_2} / (\zeta \Delta OA_y) \approx -0.01^\circ$

For the skew and the wobble, results are not very precise. the values given do not reflect reality exactly but they are in any case very low. Overall, we notice that the setup was rather well centered.

### 5.3.2 Conclusion

To conclude, we can begin by emphasizing the consistency between simulations and measurements. We find very similar values for the parameter  $\zeta$ , whether on the MLX90517 (a little more faithful) or the MLX90510. This means that the influence of the mechanical tolerances is identical to the simulations. Same thing for signal strength, the conditions of use are the same in both cases. For On-axis precision, there are notable but explicable differences, especially after calculating the positioning errors of the setup. Despite these differences, the measurement error after calibration remains acceptable.

Then the performance of the MLX90517 is very similar to that of the MLX90510, whether these sensors are calibrated or not. However, the calibration must be performed manually on each sensor, which can be too costly in time and energy for industrial productions. This is where the MLX90517 comes into its own. Without calibration and with a signal post process, it is possible to get very close to the performance of a calibrated MLX90510, which cannot really be used uncalibrated. However, there are some disadvantages to this choice: higher noise, and the risk of jumps in the AGC gain if it is not fixed, which cause the error values to explode. If this gain is fixed, the signal may end up being too weak in the event of an involuntary air gap variation, which will also degrade the signal, increase noise, etc.

## 5.4 O-shaped (1PP) MLX90517 and MLX90510

### 5.4.1 Measurement results and comparison with simulation

For the O\_shaped 1PP with an external diameter of 10 mm, all measurement processes are exactly the same as for the 5PP. The big difficulty that arises when handling this sensor is its size. It is very small and so is its associated target. It is therefore necessary to adapt the setup to this situation but this causes, among other things, greater wobbles and skews, and more difficulty in aligning the sensor and the target.

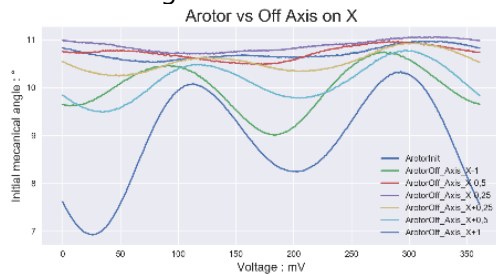


Figure 78. O\_shaped 1PP Arotor curves with X-Off\_Axis



Figure 77. 1PP target

In this case the method of alignment with Arotor previously used no longer works. The setup has too large an initial tilt, so when measuring signal strength along an x-off-axis, the initial tilt introduces an asymmetry into the error. Since the sensor is much smaller than the previous one, the nominal air gap is smaller too. In the end, in the range of usable air gap, the amplitude of the output signal of the MLX90517 is similar to the two previous sensors, with again AGC jumps. Above 1.75 mm of air gap, the sensor is no longer in these conditions of optimal use. It is a quite similar curve as in simulation, but shifted down. This indicates that the air gaps were slightly underestimated in simulation

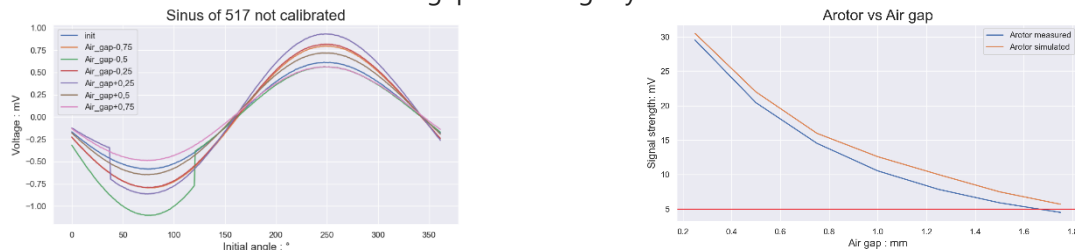


Figure 79. O\_shaped 1PP output Sinus for different Air Gap (a) and Signal strength vs Air Gap (b)

For this sensor, in the uncalibrated version, one could expect a significant error in the nominal position, but ultimately it is as precise with an air gap of 1 mm as the O\_shaped 5PP at an air gap of 5 mm. However here, improving the signal with the Min\_Max method is counterproductive: the error increases systematically. This is also linked to the nature of the output signal, which is not perfectly sinusoidal, and to the extreme sensitivity of the sensor to mechanical tolerances.

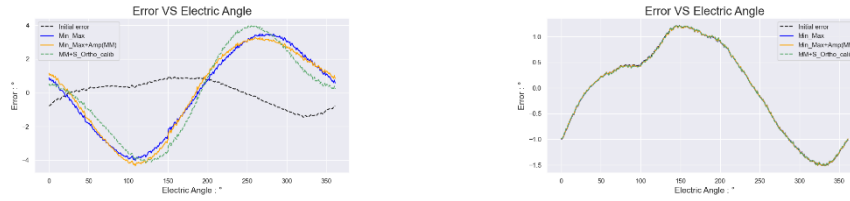


Figure 80. 72-degree average Error at nominal position for an O-shaped 1PP MLX90517(a) and MLX90510(b) uncalibrated

This sensor, however, has a particularity: calibrating it makes it less efficient. Calibrating the sensor doubles its error. This situation is created by chance placement. The mechanical tolerances of the setup compensate for certain inaccuracies of the sensor, which makes it very precise in the uncalibrated version. The error obtained with the calibration is the best possible performance for the calibration, and in these conditions, it gives surprisingly worse results.

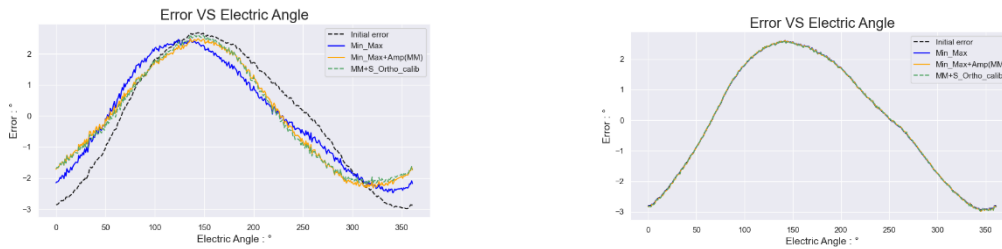


Figure 81. 72-degree average Error at nominal position for an O-shaped 1PP MLX90517(a) and MLX90510(b) calibrated

However, this error is much higher than the one found in simulation (0.6°). This shows the difficulty of designing and using this kind of small and simple sensor. In our case, a combination of non-optimal measurement conditions and some defects in the prototype make its performance poor.

Again, on this sensor too, the performance of the MLX90510 and MLX90517 is very similar. In this case, the error curves related to the variation of the mechanical tolerances are exploitable, and one can use them to find the individual contribution of tilt and off-axis to the error. The only peculiarity is that here the wobble and skew look quite important.

On the other hand, as regards the impact of air gap variations on the measurement error, the maximum values obtained are absolutely identical to the simulations.

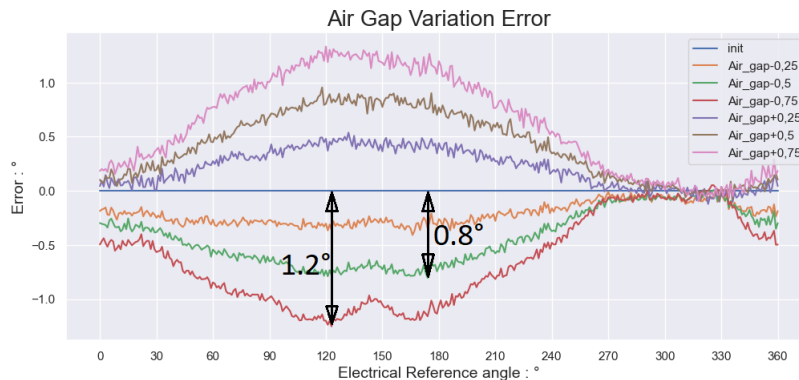


Figure 82. 360-degree periodic error in function of Air Gap variation for an O-shaped 1PP MLX90510 calibrated  
As a reminder, for this sensor, the calculation method that we applied to the 5PP is not applicable (not enough poles). Off axis and tilt have their independent contribution.

During our simulations, we obtained an off-axis (oa) contribution of  $11.16^\circ$  and a tilt-related (t) contribution of  $2.06^\circ$ . These contributions are names sensitivity.

For the off-axis sensitivity:

We apply an additional x off-axis  $\Delta OA_x = +0.5\text{mm}$ . Error induced:  $\Delta \epsilon_1 = \text{sensitivity}_{oa_x} = 9.47^\circ$  (2\*peak to peak error/2)

Thanks to the sinusoidal approximation, we realize that in reality the error curve is not sinusoidal and which confirms that the previous method is not applicable.

Also, we apply an additional y off-axis  $\Delta OA_y = +0.5\text{mm}$ . Error induced:  $\Delta \epsilon_2 = \text{sensitivity}_{oa_y} = 9.47^\circ$

We therefore obtain a global sensitivity<sub>oa</sub> of  $9.5^\circ$  perfectly symmetrical which is a value 25% lower than in simulation, the sensor is therefore less sensitive to off axis variations than expected.

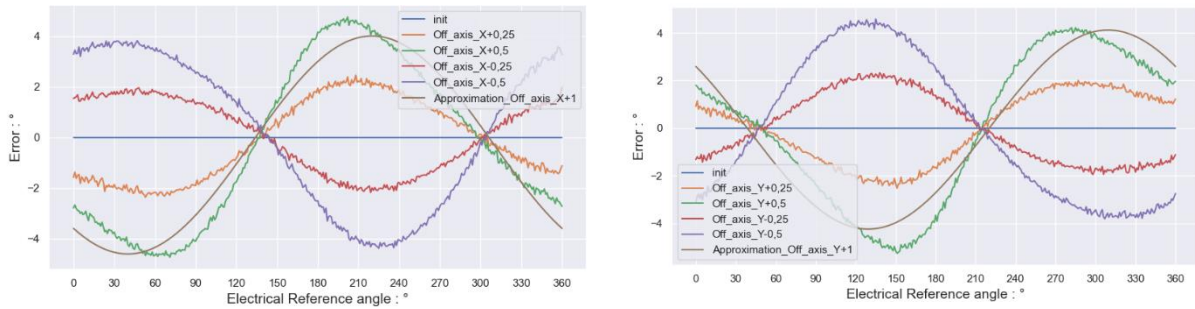


Figure 83. 360-degree periodic error in function of x-off-axis (a) and y-off-axis (b) variation for an O-shaped 1PP MLX90510 uncalibrated with approximation

For the tilt sensitivity:

We apply an additional x tilt  $\Delta T_x = +0.5^\circ$ . Error induced:  $\Delta \epsilon_3 = \text{sensitivity}_{t_x} = 4.79^\circ$

We apply an additional y tilt  $\Delta T_y = 0.5^\circ$  or  $-0.5^\circ$ . Error induced:  $\Delta \epsilon_4 = \text{sensitivity}_{t_y} = 4.52^\circ$  for  $\Delta T_y = 0.5^\circ$  or  $= 4.53^\circ$  for  $\Delta T_y = -0.5^\circ$  (quite symmetrical measurement).

We therefore obtain an average sensitivity<sub>t</sub> of  $4.7^\circ$  with small differences between the two axes. This is a value 28% higher than in simulation, the sensor is therefore more sensitive to off axis variations than expected.

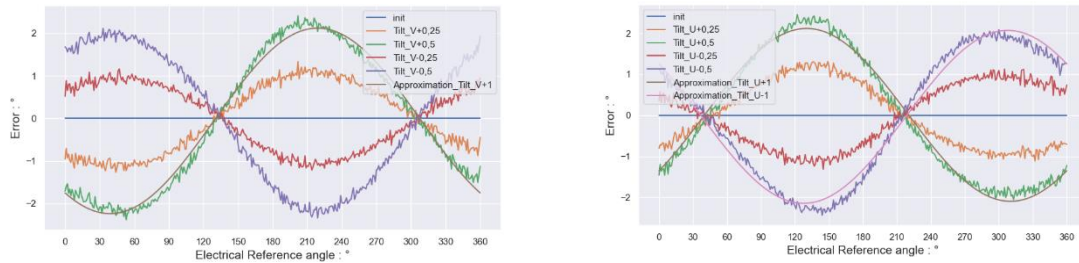


Figure 84. 360-degree periodic error in function of x-tilt (a) and y-tilt (b) variation for an O-shaped 1PP MLX90510 uncalibrated with approximation

### 5.4.2 Conclusion

The measurements are overall quite symmetrical, but with important differences compare to simulations. This sensor, still in the prototype state, is too sensitive to mechanical tolerances, it very often loses the signal during the measurements, which greatly deteriorates their interest and their precision. In the current state of the sensor, the simulations are not very faithful to the real behavior of the sensor on all points, which is a point of notable possible improvement.

This does not mean that the simulations are irrelevant. Unfortunately, the setup was difficult to align and large unintended initial mechanical tolerances are the cause of these discrepancies.

Regarding the MLX90517, for this sensor it is of no apparent interest. The Min\_Max method is useless and a MLX90510 will always have better performance.

## 5.5 C-shaped (5PP) MLX90510 and MLX90517

### 5.5.1 *Measurement results and comparison with simulation*

For the C\_shaped with an external diameter of 114 mm, all measurement processes are exactly identical. However, for this case, the sensor is no longer symmetrical. The method to align the sensor and the motor no longer works correctly (because there is only one axis of symmetry). In addition, this sensor is enormously more sensitive to mechanical tolerances, which creates large error peaks in the measurements.

One of the first remarks that can be made concerns the amplitude of the output signal in MLX90517 mode. Indeed, it is similar to that of the O\_shaped 5PP and here we find even more problems related to AGC jumps as can be seen in the following graph (SinAir\_gap+3 before 750° and after 1750°). Moreover, because of the shape of the sensor and certain internal amplitude modulations linked to this type of sensor, the signal is not perfectly sinusoidal, which will pose problems for working on it.

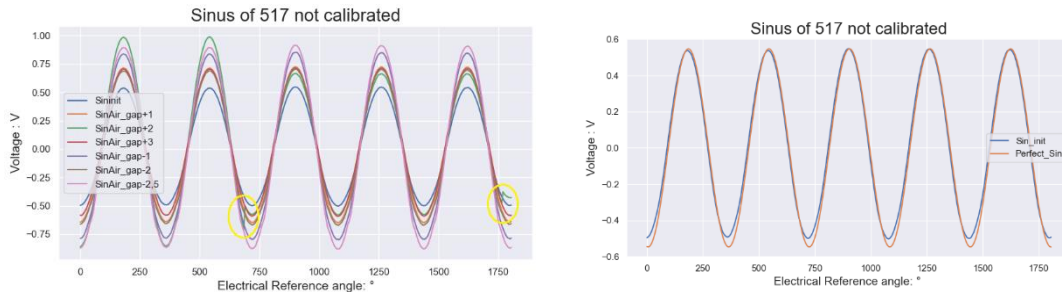


Figure 85. *C\_shaped 5PP Output Sinus for different Air Gap (a) and output initial sine vs a perfect sine (b)*

As for the O\_shape, we can plot the measurement error curve associated with the nominal position, and apply the Min\_Max method to it.

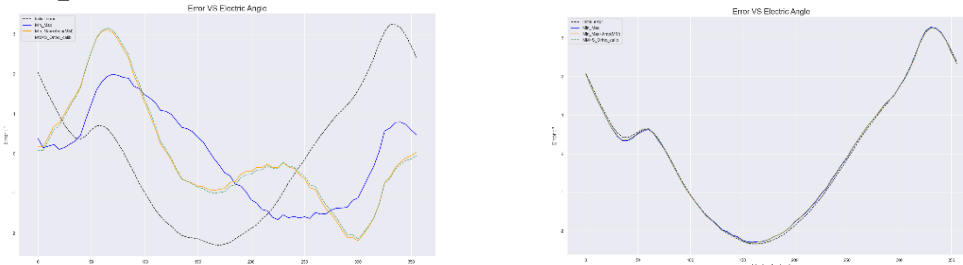


Figure 86. *72-degree average Error at nominal position for a C-shaped 5PP MLX90517 (a) and MLX90510 (b) uncalibrated*

As we can see, the Min\_Max method is absolutely not efficient as it is for the O\_shape. For the MLX90510 it is useless as expected. However, for the MLX90517, it can amplify some error peaks and reduce others. Its effectiveness is therefore less and random (Depending on the residual mechanical tolerances, it can amplify the error or reduce it). Worse still, if we try to normalize the amplitude, we increase the error every time. For this type of sensor, it is necessary to question the relevance of using an MLX90517.

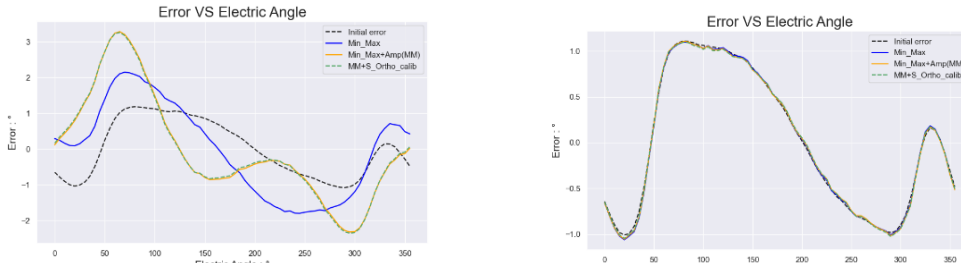


Figure 87. 72-degree average Error at nominal position for a C-shaped 5PP MLX90517(a) and MLX90510(b) calibrated

All these remarks are also valid when the sensor is calibrated. To compare it to the O-shaped, we note that uncalibrated, it can display doubled measurement errors, and that here the calibration is much less efficient than for the O-shaped 5PP, in our case it only divides the error by 2.4 (versus 10 for the O-shaped 5PP).

In simulation, in nominal condition, the sensor displayed a peak-to-peak measurement error of 0.8°. Here the error is about 2° which is more than double. Again, and as for the O-shaped 1PP, the geometry of the sensor makes it very difficult to center, and therefore to operate in optimal conditions. Real measurements show us that the conditions in which the sensor is simulated are difficult to recreate in real use.

However, as with the other two sensors, the signal strength figure is identical to the simulations. The optimal conditions of use are at air gaps of less than 4mm

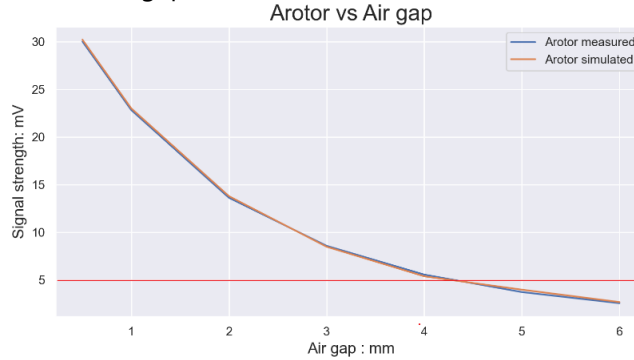


Figure 88. C-shaped 5PP signal strength vs Air Gap

As for the influence of air gap variations on the error curves, the results are as chaotic as in simulation with quite different behavior overall. Above all, there is a strange fact that appears: By bringing the sensor very close to the target, there are huge error peaks that appear periodically. This behavior was not predicted by the simulations and is largely due to the internal amplitude modulations that a C-shaped must perform to reconstitute a clean signal. On the other hand, by increasing the air gap, the prototype is less sensitive than in simulation.

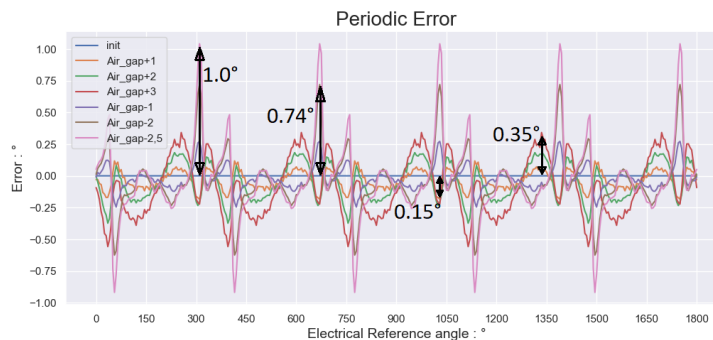


Figure 89. 360-degree periodic error in function of Air Gap variation for an C-shaped 5PP MLX90510 calibrated

As for the O\_shaped 1PP, each mechanical tolerance alone contributes to the measurement error. Here are the measurements that can be compared to the simulations. Unlike O\_shapes, here the error curves really don't approach sinusoids.

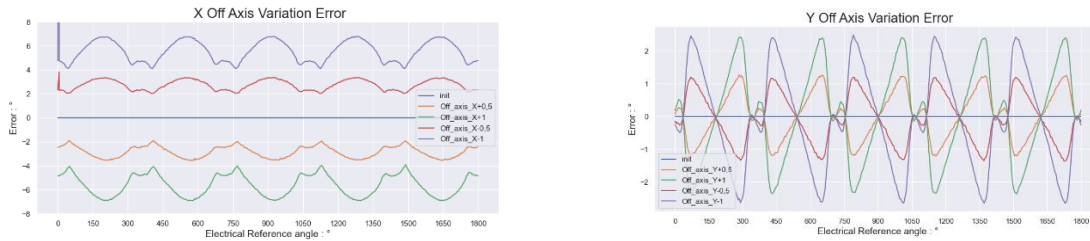


Figure 90. 360-degree periodic error in function of x-off-axis (a) and y-off-axis (b) variation for a C-shaped 5PP MLX90510 uncalibrated

The simulated values here correspond to the green curves (+1). For the x-off-axis, we find this strong negative offset linked to the asymmetry that this mechanical tolerance creates. Its shape is very similar to the simulations in which we found a maximum value of 6.5° in absolute value. Here it is slightly more: 6.9°. For the y-off-axis, it is perfectly symmetrical and of zero mean value as during the simulations. Indeed, here no asymmetry is created. Only the surface of the measured target changes. In simulation the maximum value of the error was 2.3° and here too, for the measurements it is a little higher: 2.4°.

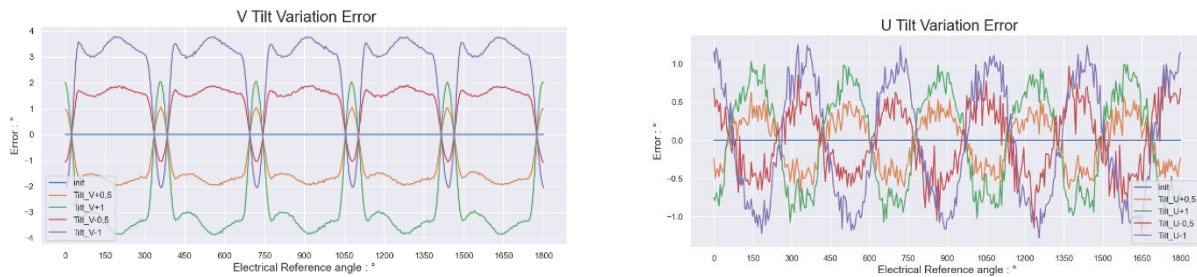


Figure 91. 360-degree periodic error in function of x-tilt MLX90510 (a) and y-tilt MLX90517 (b) variation for a C-shaped 5PP uncalibrated

The measured error caused by an off axis is slightly underestimated by the simulations. However, for the Tilt it is a bit different. The x-tilt (V here) has an identical form to the simulation: a fairly constant negative value and a large positive peak. Nevertheless, in simulation, this value fell to the lowest at -1.7° and the peak rose to 3.9°. Here during the measurements, the low value is -3.8°, and that of the peak is 2.0°. In peak to peak, as for the off axis, the measured error value is a little underestimated by the simulation, but here there is a shift of the offset of 2.1° negatively that the simulation does not foresee.

This behavior is certainly due to an initial and unwanted tilt on the measurement setup at the initial position: the value of the offset does not evolve linearly. For the y-tilt (U here), we find as in simulation an average value of the error almost zero but the peak-to-peak value is more than doubled (2.0 here, 0.8 in simulation), which is also due to a defect of setup alignment. For this case, the data from the MLX90517 had to be used because the measurements on the MLX90510 on this mechanical tolerance were affected by measurement problems.

However, an effect that has not been simulated appears here: the error created by a negative y-tilt is very different from that created by a positive y-tilt. Indeed, it is only a change in the surface of the target detected by the coils but the positive tilt brings the target closer to the sensor while the negative tilt moves it away. Hence this difference.

### 5.5.2 Conclusion

To conclude we can say that the behavior of C\_shaped is very similar to what was simulated. The measurements just show that these simulations slightly underestimate the error caused by all the mechanical tolerances. As for the O\_shaped 1PP, these differences are largely explained by the non-perfect alignment of the setup during the measurement campaigns. This sensor is as expected much less efficient than the O\_shaped 5PP and because of certain internal amplitude modulations, the use of the MLX90517 does not make much sense because the Min\_Max method is useless.

The C\_shaped is much cheaper than an O\_shaped but its low accuracy and the inefficiency of the MLX90517 mode are major weakness.

## 5.6 Conclusion

To conclude on the shape of the sensors, it is obvious to say that an O\_shaped with a number of poles higher than 2 and diameter higher than 25mm will always have a clear advantage in terms of performance and consistency between simulations and real use. Although the C\_shaped is much less expensive, their extreme sensitivity to mechanical tolerances as well as their internal amplitude modulation make them much less efficient products than the O\_shaped of similar size.

As for the MLX90517, its relevance is quite limited in shape and size of sensor, for a classic O\_shaped like the one studied it is obviously a fully conceivable solution despite these few faults (including noise and gain problems) but for a C\_shaped or a small O\_shaped is a counterproductive solution.

One of the points that I did not address concerns the effect of speed on the sensor. Indeed, problems related to the propagation delay on the high-speed measurement setup made it difficult to use certain data. However, there are some interesting things to say about it.

Measurements made at high speed inevitably induce a propagation delay. Between the moment of the measurement, and the moment when the information is available at the output of the sensor, the angle has changed. One of the notable advantages of the MLX90510 is that it predicts the value of the future angle over a short period of time as a function of the measured speed and acceleration. This compensates for this propagation delay. This is one of the big advantages of this sensor compared to those of the competition. On average, we find a maximum propagation delay of 4  $\mu$ s with the competition, while it is 120 ns with Melexis. This effect is especially observable at high speed and high temperature.

## 6 Conclusions and perspectives

---

### 6.1 Conclusion

In conclusion, I can say that we have fulfilled the objectives of this internship. I performed a full-blown analysis of the accuracy of inductive position sensors, studied and compared the MLX90510 and the MLX90517 interface IC for position measurement and also proposed different algorithms to improve performance of each approach with some success. There is one point that I haven't really had time to address during these six months, which concerns the comparison of Melexis sensors with those of the competition in their design. This is work that I had underestimated and it deserves a report on its own. It is surely a job that I will undertake once truly installed in the team.

From now on, thanks to my job, Melexis engineers can use my data to analyse in more depth certain behaviours of the sensors they develop as well as have a more global view of the interest of a MLX90517 or MLX90510 configuration in relation to customer expectations.

Currently, the inductive team at Melexis is evolving. It was made up of two members last year, three this year and we will be four at the start of the next school year with my new arrival. The number of clients and projects are increasing which is as exciting as it is challenging. In addition, I have a lot of ideas to bring to this team to help it move forward. Improve the stability of O\_shaped 1PP measurements, integrate an automatic calibration system directly into the sensor IC, or even integrate Min\_Max in a variant of the MLX90517.

I think that this work fits perfectly into the philosophy of the engineer: search, solve, facilitate, understand, upgrade.

### 6.2 Personal review

I personally enjoyed working on this project a lot. It is directly linked to the subjects I study in Grenoble as well as in Turin (electronics, sensors, testing...) but requires skills that have never been taught to me. I enjoyed doing research, learning on my own, and building my project as I saw it. I didn't know what my job was going to look like when I started this internship and I'm glad with the result. I managed to perform measurements, compile and analyze data which is already useful to the engineers of the inductive team to better understand the behaviour of some of the sensors they are developing and the interest of the MLX90517 with regard to performance and ease of use of the MLX90510 and I'm proud of it.

I have the feeling of having worked for 6 months in a field that I like, in a company that I like and in a position that interests me. This makes me confident for my new life as a future graduate and new Melexis employee.

## 7 Bibliography

---

- [1]. Brajon, B. (2020). *Development of a Hybrid Magnetic-Inductive Angular Sensor With 360° Range And Stray Field Immunity*. Rome.
- [2]. Infineon. (2018). *TLE5xxx(D) Calibration 360°*. Munich: Infineon.
- [3]. Lugani, L. (2020). *O\_shaped\_coils\_based\_inductive\_sensors*. Bevaix: Melexis.
- [4]. Lugani, L., Akermi, Y., Laval, P., & Duisters, T. (2021). *High speed inductive position sensor for E-machines*. Bevaix: Melexis.
- [5]. Melexis. (2021). *MLX90510 High-Speed Inductive Position Sensor Application Note*. Bevaix: Melexis.
- [6]. Melexis. (2022, 08 10). *about-us*. Retrieved from melexis.com:  
<https://www.melexis.com/en/about-us>
- [7]. Melexis. (2022, 08 10). *High-speed inductive resolver with analog output*. Retrieved from melexis.com:  
<https://www.melexis.com/en/product/MLX90510/High-Speed-Inductive-Resolver-Analog>